

<https://doi.org/10.1038/s43247-024-01296-9>

Intensification and shutdown of deep convection in the Labrador Sea were caused by changes in atmospheric and freshwater dynamics

Check for updates

Igor Yashayaev

Labrador Sea winter convection forms a cold, fresh and dense water mass, Labrador Sea Water, that sinks to the intermediate and deep layers and spreads across the ocean. Convective mixing undergoes multi-year cycles of intensification (deepening) and relaxation (shoaling), which have been also shown to modulate long-term changes in the atmospheric gas uptake by the sea. Here I analyze Argo float and ship-based observations to document the 2012–2023 convective cycle. I find that the highest winter cooling for the 1994–2023 period was in 2015, while the deepest convection for the 1996–2023 period was in 2018. Convective mixing continued to deepen after 2015 because the 2012–2015 winter mixing events preconditioned the water column to be susceptible to deep convection in three more years. The progressively intensified 2012–2018 winter convections generated the largest and densest class of Labrador Sea Water since 1995. Convection weakened afterwards, rapidly shoaling by 800 m per year in the winters of 2021 and 2023. Distinct processes were responsible for these two convective shutdowns. In 2021, a collapse and an eastward shift of the stratospheric polar vortex, and a weakening and a southwestward shift of the Icelandic Low resulted in extremely low surface cooling and convection depth. In 2023, by contrast, convective shutdown was caused by extensive upper layer freshening originated from extreme Arctic sea-ice melt due to Arctic Amplification of Global Warming.

The Labrador Sea is the coldest (Fig. 1) and freshest deep subpolar North Atlantic (SPNA) basin¹ where intense vertical mixing driven by high winter surface heat losses (WSHL) produces Labrador Sea Water (LSW)—a major North Atlantic intermediate-depth water mass^{2–8}. Cold fresh dense oxygen-rich LSW spreads across the ocean renewing and ventilating its intermediate and deeper layers^{9–15}. The LSW formation process, *deep convection*, defines interannual and longer-term trends in these layers^{15–20}, spins the North Atlantic Subpolar Gyre²¹ and affects the exchanges between the Subpolar and Subtropical Gyres^{22,23}. LSW enters^{19,24} and, arguably, controls^{25,26} the lower limb of the Atlantic Meridional Overturning Circulation (AMOC).

The contribution of the Labrador Sea to the AMOC was recently challenged by the Overturning of the Subpolar North Atlantic Program (OSNAP), reporting it to be much lower²⁷ than, e.g., the volumetrically-defined LSW export⁷. It should be noted that there are arguable reasons for an underestimation of the Labrador Sea contribution based on the OSNAP

observations. Only a few of these reasons are given below. The interior LSW recirculation and exit flows, present on the seaward sides of the moorings, are not accounted for by the OSNAP array. LSW spreading from the Labrador Sea (Fig. 1d, e) to the Irminger Sea and Iceland Basin^{10–12} is entrained by the boundary currents and dense overflows in vicinities of the continental slope and rise, and Mid-Atlantic Ridge¹⁹, thus contributing to the AMOC outside the LSW source (the entrainment of LSW by the Iceland–Scotland Overflow Water will be revisited in the “Results” section). Located outside the deep convection zone in the central Labrador Sea, the OSNAP array is exposed to convection in the eastern part, reducing the Labrador Sea contribution there. Lacking vertical resolution and accuracy, the mooring-based density measurements underestimate the LSW thickness changes entering the transport calculations. Identifying and understanding the limitations, omissions, and inconsistencies in the OSNAP observations will allow us to address and resolve the controversies in results and improve the program design.

Bedford Institute of Oceanography, Dartmouth, NS, Canada. e-mail: Igor.Yashayaev@dfo-mpo.gc.ca

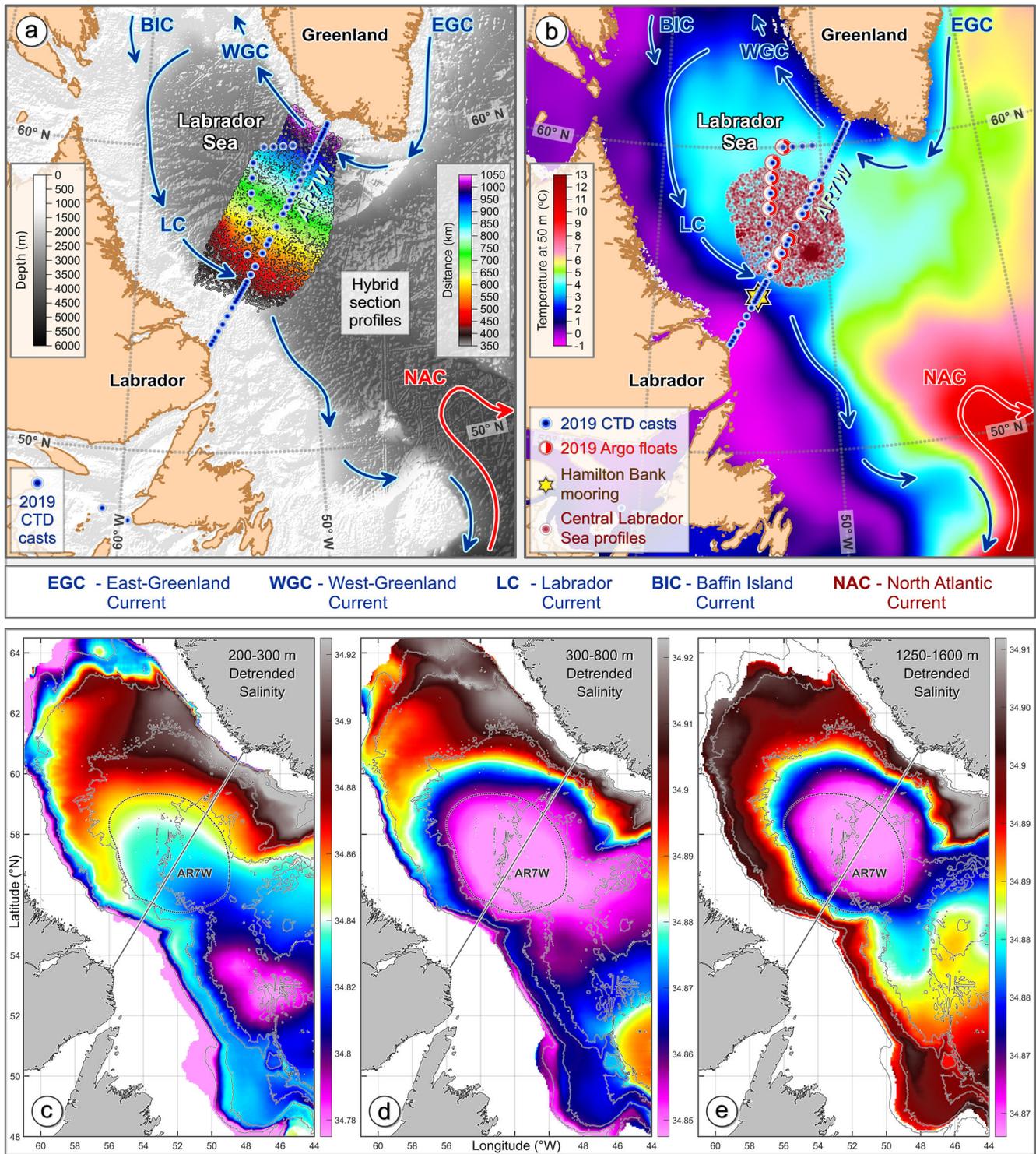


Fig. 1 | Oceanographic features of the Labrador Sea and hydrographic data sources used in this study. The key topographical features (a), temperature climatology at 50 m depth (b) and major upper currents of the Labrador Sea. The locations of the 2019 Argo float deployment (a), oceanographic station (a, b), and Hamilton Bank mooring (b; ~1000 m depth). The locations of the float and ship-based measurements used to construct the composite seawater property sections (a; color-coded by distance) and central Labrador Sea time series (b; dark red). Maps of the de-

seasoned, low-pass filtered, and averaged, first vertically over the 200–300 m (c), 300–800 m (d), and 1250–1600 m (e) layers, and then over overlapping spatial bins, 2002–2023 Argo float and ship-based salinity values (the steps followed to construct these maps are further explained in Supplementary Note 4). The Central Labrador Sea region and AR7W repeat hydrography line are indicated with black dotted and gray lines, respectively (c–e), and bathymetric contours are shown in the background.

The role that Labrador Sea convection plays in freshwater and, analogously, atmospheric gas uptake by the deep ocean is reflected in the salinity maps shown in Fig. 1c–e and Supplementary Figs. 6–8. The low-salinity (high freshwater content) zone becomes more localized with depth,

revealing the epicenter of deep convection. Because of this unique ability to sequestrate freshwater and atmospheric gases below 1000 m, the Labrador Sea is regarded as a source region in larger-scale studies. The LSW production and export were shown to play a vital role in the planetary carbon

and biochemical cycling by intaking the atmospheric gases^{28,29}, and by controlling deep bacterial biomineralization³⁰. Labrador Sea convection transfers nutrients from the deep layers to the surface, consequently sustaining primary production in the euphotic zone of the Labrador Sea²¹. Ultimately, the named processes affect the multi-level biological productivity and ecosystem well-being across the northeastern North Atlantic³¹.

Each multiyear convective cycle comprises the phases of progressively deepening convection and convective relaxation. The former is initiated and upheld by high WSHL leading to the production of incrementally cold dense deep massive LSW. The latter is dominated by generally weak and shallow convection leading to reduced or suppressed LSW production. The voluminous LSW classes, developed by recurrently deepening convection, are distinguished by their unique oceanographic characteristics, including density, temperature, salinity, dissolved oxygen, and potential vorticity^{7,8}. The multiyear convective cycles dominate the decadal and longer-term variability of seawater properties in the intermediate and deep layers of SPNA^{5,7,16,20}. Both record-large, 1987–1994, and smaller, 2000–2003, LSW classes⁷ arrived at Bermuda and Abaco locations 10-to-15 years after formation¹⁵. The deep boundary current speed off Cape Hatteras also increased in response to the 1987–1994 LSW development²⁶.

Detailed inventories of individual convective cycles, containing high and low points, LSW properties, and volumes, provide critical benchmarks and references for large-scale variability, connectivity, and circulation studies, including follow-up investigations of the ocean-wide spreading, mixing, and transformation of water masses. The present study documents and analyzes every significant detail of the last, 2012–2023, convective cycle. It was formerly hypothesized that the 2012–2016 intensification/deepening of convection preconditioned the water column to be susceptible to deeper convection in the following years even under moderate atmospheric forcing^{7,8}, boosting the decadal LSW volume to the highest since the mid-1990s. This hypothesis is tested here, and the causes of the recent convective shutdown are investigated, answering the following questions:

- (1) How can year-to-year varying net surface cooling, water-column preconditioning, seasonal restratification, and sustained stratification buildup (e.g., freshening-driven) be compared and ranked by their contribution to the deepening/shoaling of winter convection?
- (2) What are the oceanic and atmospheric phenomena, processes, and mechanisms responsible for the recent switchovers in convective activity in the Labrador Sea?
- (3) What is the origin of the present freshening of the Labrador Sea? How does its magnitude compare to the previous salinity anomalies?
- (4) How can the 2012–2023 convective cycle be ranked relative to the most massive multiyear LSW production and oxygen uptake on record?

Results

Composite hydrographic sections for April–August of 2018–2023

Even though the *central Labrador Sea* (CLS), which I define as the region where deep convection is likely to occur (Fig. 1c–e and Supplementary Figs. 6–8), is in focus of this study, we first visually assess the vertical and horizontal uniformity of LSW in the post-convective periods of the last 6 years, 2018–2023. This task is achieved by comparing the section plots built in the following way. The *hybrid-coordinate method* of projecting scattered points on an arbitrary line, as explained step-by-step in the “Methods” section, was applied to the quality-controlled, calibrated, and vertically interpolated Argo float and ship-based observations, henceforth, *hydrographic observations*, to construct the vertical sections presented in Fig. 2. The vertical profiles, which positions are indicated in Fig. 1a with respective section distance color-coded dots, were projected on the Atlantic Repeat hydrography line 7-West (AR7W) crossing the Labrador Sea from *Misery Point*, Labrador, to *Cape Desolation*, Greenland. The year-specific sections brought for this comparison depict the basin-wide hydrographic conditions averaged for the spring-summer periods of the respective years, ranging from April, with the newly-formed fully-developed nearly-intact LSW vintages, to August, with the same vintages in approximately half-

volume half-modified states achieved through mixing and export. The annual composite sections lined up in Fig. 2 exhibit some of the most rapid interannual changes observed over three decades. It is also important to note that the composite vertical profiles (discussed later) and sections for 2021 are entirely Argo-based. 2010–2023 full-depth AR7W transects (Supplementary Figs. 2–4) depict random-time sea-wide conditions.

Formed in 2018, LSW₂₀₁₈ (subscripts in Fig. 2 year-tag annual LSW vintages) stands out as a cold dense blob nested between 700 and 2000 m. It is the coldest, densest, deepest, and most voluminous LSW vintage since 1995 (Figs. 2–5, 8, 10, and Supplementary Figs. 2–4). Winter convection weakened in 2019, barely reaching 1400 m in the western part, while being much shallower than that in the rest of the basin. The shoaling of convection resulted in the coexistence of LSW₂₀₁₉ and LSW₂₀₁₈ in 2019. In 2020, convection deepened to 1600 m, cooling the 200–2000 m, henceforth, *intermediate*, layer. The situation radically changed in 2021: its winter convection shoaled to 800 m; the cold layer of remnant LSW₂₀₂₀, seen only below 800 m, thinned by 500 m from the previous year (when LSW₂₀₂₀ was formed); while the whole intermediate layer, especially its upper half, warmed. Furthermore, in 2021, salinity substantially decreased in the layer above 800 m and increased in the layer below. The rapid sea warming and convection shoaling observed in 2021 were partially offset next year as winter cooling and convection reintensified. However, the upper-layer freshening persisting since 2021 prevented convection from reaching the depth expected from the cooling along (as shown below). In 2023, the sea-wide freshening dominated the top 700 m layer, disrupting deep convection for the second time in 3 years.

A high-resolution observational record of convective developments in the Labrador Sea

Having assessed the spatial extent of the water masses formed by winter convection in the recent years (2018–2023), we now switch our attention to high-resolution time series revealing both seasonal development and year-by-year evolution of winter mixing, followed by post-convective restratification. This level of mapping and hence understanding of the processes in the deep ocean became possible only with the inclusion of the International Argo Program data in the ongoing research (see the “Methods” section and Supplementary Notes 4–6).

The CLS *hydrographic observations* (Fig. 1b, *dark-red dots*) are time-bin-averaged with the high temporal resolution to map seasonal-to-decadal variability in the 0–2000 m layer, including all convective developments, highlighted by the density-layer thickness changes, since 2002 (Fig. 3). The CLS data selection and processing steps are outlined in the “Methods” section.

The most recent development of progressively deepening winter convection, ventilation, cooling, and densification of the Labrador Sea spanned the entire 2012–2018 period. It was preceded by relatively weak and shallow 2010 and 2011 winter mixing events (620 and 820 m, respectively), and initiated by a 1300 m deep convection in 2012. Recurrently deepening to the point of reaching 2000 m in 2018, this multiyear convective development produced LSW_{2012–2018}—the coldest densest, and largest LSW class so far in this century (subscripts in Fig. 3 indicate the year ranges of the prominent LSW classes developed since 2000).

The phase of recurrently intensifying and deepening convection ended in 2018. It was followed by the convective relaxation phase, ultimately completing the multiyear convective cycle. Convection shoaled after 2018, making the intermediate layer warmer and less dense (Figs. 2–4 and Supplementary Figs. 2–4, 17–22). The relaxation reached its first peak in 2021, when convection rapidly shoaled to 800 m forming a thin warm low-density (potential density, σ_t , referenced to 1000 dbar, henceforth, *density*) mixed layer. In 2022 convection penetrated twice deeper than in 2021. However, the ongoing convective relaxation phase was not reversed by that event. Moreover, being >100 m shallower than the already shallow convection of 2021, the weak, <700 m deep, convection of 2023, boosted the rate of convective decline to record high. Also, to support the explanation of the most recent shutdown of deep convection given later in the “Results”

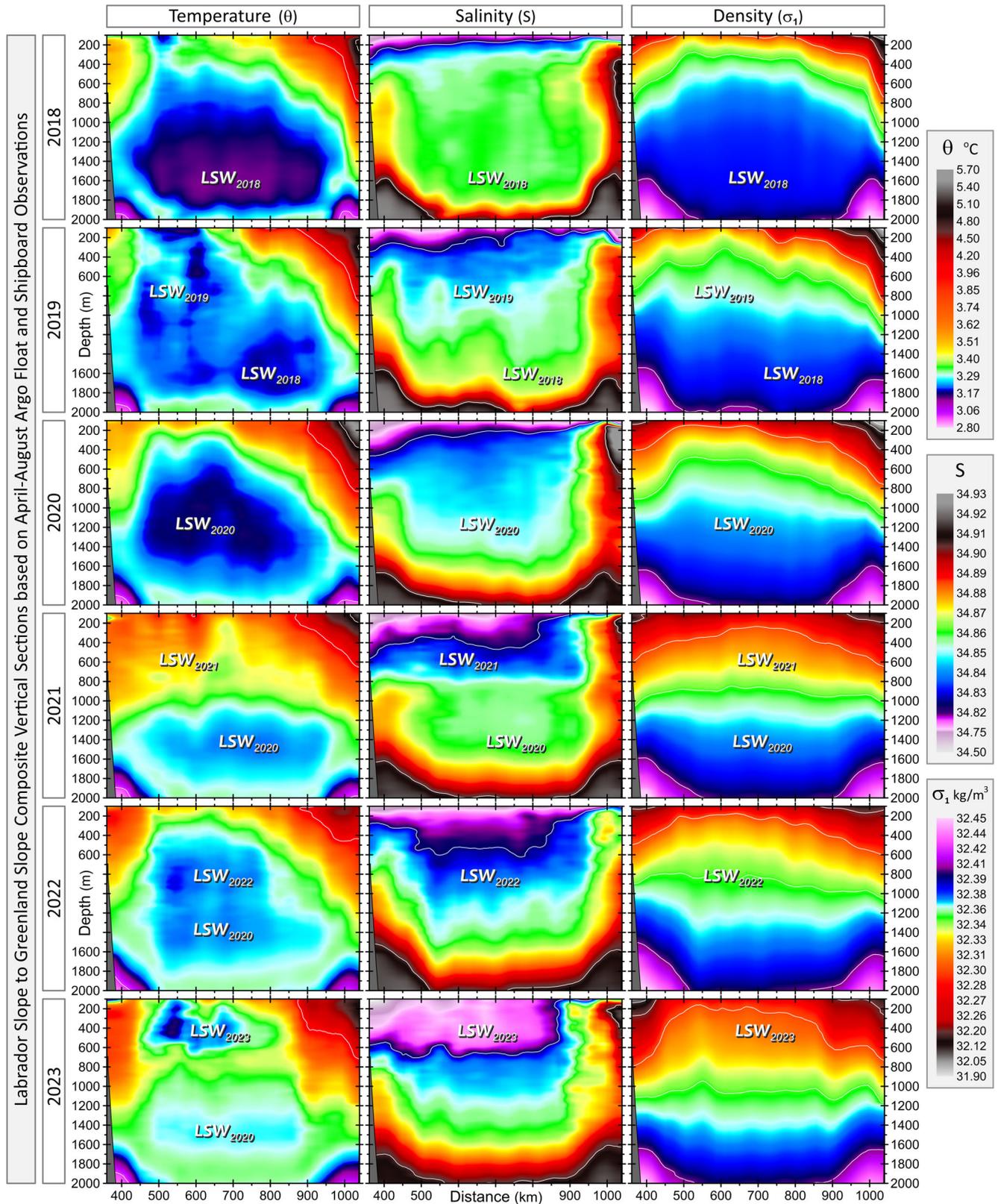


Fig. 2 | 2018–2023 post-convective (Apr–Aug) composite temperature, salinity, and density sections. Labrador Sea Water vintages are indicated by LSW, their formation years are subscripted.

section, please note that despite being the shallowest in 13 years, the 2023 winter mixed layer turned out to be a cold one. Particularly, the winter mixed layer of 2023 was much colder than the mixed layer of 2021, meaning different mechanisms of convective shutdown in 2021 and 2023.

The ongoing freshening of the Labrador Sea revealed by the basin-wide April–August composites (Fig. 2) stands out in the time series of vertical salinity profiles as the largest freshening event of the past two decades (Fig. 3). The stepwise deepening of the 34.84 isohaline reflects

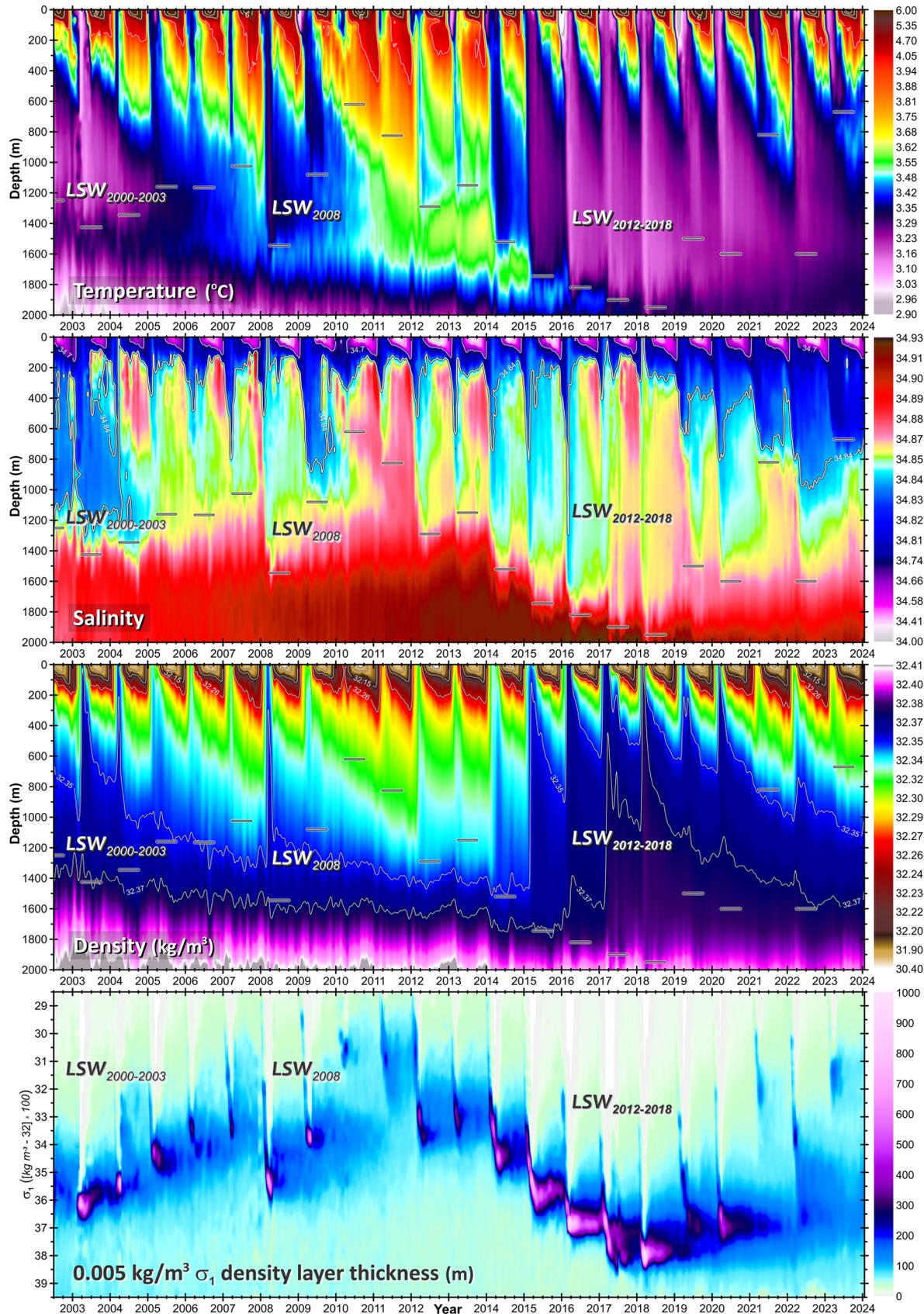


Fig. 3 | 2002–2023 central Labrador Sea temperature, salinity, density, and 0.005 kg/m^3 density layer thickness based on quality-controlled and calibrated Argo float and ship-based observations. Short horizontal lines indicate the convection depths. LSW subscripts denote year classes.

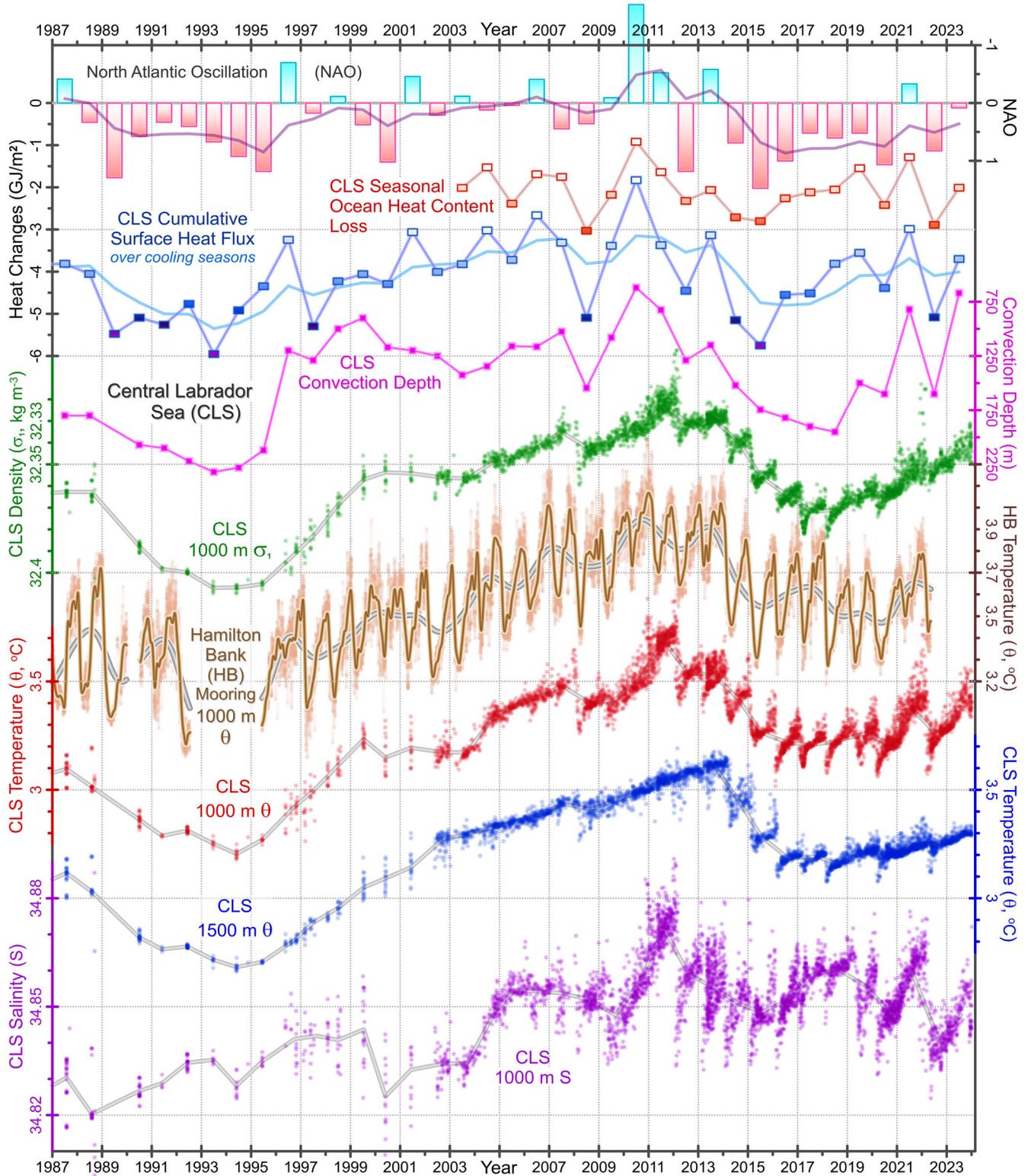


Fig. 4 | Footprints of winter surface cooling in deep temperature, salinity, and density. *Top-down:* The winter NAO index (*inverted bars*); the central Labrador Sea (CLS) 15–2000 m layer (*red*) and cumulative surface (*blue*) heat flux, the convection depth (*violet*), the Argo float and ship-based 1000 m density (σ_1 , *green*), temperature

(θ , *red*), and salinity (*S*, *purple*), and 1500 m θ (*blue*), acquired through 2023–Aug-31, and respective annual averages (*connected with gray lines*); the Hamilton Bank (HB) mooring 1000 m bottom low-pass filtered θ (*brown*).

the persistent multiyear development and deepening of this event: firstly deepened from ~150 m in mid-2017 to ~250 m in mid-2018, it continued to deepen annually until reaching 1000 m in 2022. Here again, 2021 shows some exceptional features, like its 200–800 m layer average

salinity decrease and freshwater content increase rates being among record highs. Furthermore, its winter mixed layer depth of ~800 m served as a barrier separating the overlaying freshened and underlying salinized parts of the intermediate layer. As convection deepened in 2022, the

freshening entered the 1000–2000 m, *deep intermediate*, layer. This freshening will be presented below as one of the deep-convection preventers in the Labrador Sea.

The recent multiyear convective cycles, including their intrinsic gradual, rapid or abrupt transitions or switchovers from recurrent intensification to relaxation and shutdown of convection, and the key characteristics, including depth, thickness and volume, of all annual LSW vintages can be accurately identified, assessed and tracked following the evolution of $0.005 \text{ kg/m}^3 \sigma_1$ layer thickness peaks and ridges in the σ_1 -time coordinates (Fig. 3). Each annual LSW development shows there as a ridge of the thicker layers, henceforth, *pycnostads*, confined to 0.005 kg/m^3 wide σ_1 ranges centered at particular σ_1 values. The annual pycnostads thin out following their winter formation periods, reflecting the export and replacement of the associated LSW vintages, and possibly some diapycnal mixing during the restratification season. The LSW_{2000–2003}, LSW₂₀₀₈, and LSW_{2012–2018} classes are identifiable as the thicker pycnostads. The longest progression of closely spaced continually densifying and thickening pycnostads tracks the development of the LSW_{2012–2018} class. Following this development, the Labrador Sea entered a convective relaxation phase. Indeed, the annual pycnostads were generally thinner, weaker, and more varying in σ_1 over 2019–2023 than in the five previous years. The 2002–2023 period's weakest, shallowest, and least dense pycnostads were formed in 2010 and 2011, and in 2021 and 2023, setting the beginning and the end of the last full convective cycle.

What are the atmospheric factors controlling Labrador Sea winter cooling and convection?

Considering that of the three processes controlling the strength, duration, and depth of convection, namely atmospheric forcing, convective preconditioning, and post-convective restratification, the winter atmospheric forcing is both initiator and lead actor, we first define the metrics of its strength.

Figure 4 includes three important metrics of the winter atmospheric forcing and its direct impact on the Labrador Sea heat content: the winter *North Atlantic Oscillation* (NAO) index³² representing large-scale atmospheric circulation modality associated with the average subpolar North Atlantic zonal flow; opposite to WSHL, the net CLS sea-to-air heat fluxes (heat losses) integrated over the individually defined seasons of prevailed surface cooling; and the 15–2000 m layer heat content losses experienced by CLS over the individually defined 2003–2023 cooling seasons (henceforth, 2003 refers to the 2002–2003 cooling season, etc.). The heat losses incurred by the water column are highly correlated with the winter surface heat losses and NAO indices of the respective year. The correlation coefficient of ~ 0.9 for 21 independent samples (years) supports the conclusion that the atmospheric forcing dominates the winter heat content changes integrated over the 15–2000 m layer of the Labrador Sea.

The NAO and WSHL series were also non-recursively low-pass filtered with a *five-year left-side triangular* time window. This filter window, specifically for this task, had its weights increasing linearly from 0.2 at the fourth preceding point to 1.0 at the current state point, with no future states entering the filter, meaning that only the current (rightmost) and four past (left-side) states are weight-averaged. The resulting low-pass filtered series (Fig. 4, *overlain solid lines*) represent the combined effects of the past and present winter atmospheric forcing on the present oceanic conditions (e.g., convection depth, heat content), assuming a linear decline over time.

Besides the winter forcing metrics shown in Figs. 4, 5e, f shows the winter *Arctic Oscillation* (AO)³³, also referred to as *Northern Hemisphere annular mode*, index. The AO index reflects the intensity of the tropospheric circum-Arctic circulation, possibly associated with the tropospheric polar vortex (TPV). TPV is the tropospheric counterpart of the *stratospheric polar vortex*, commonly referred to as the *polar vortex* ([henceforth, *Northern Hemispheric*] PV). PV is associated with a depression in the wintertime 50 mbar geopotential surfaces (Supplementary Fig. 23). TPV and PV have different sizes (the former is much larger than the latter, Supplementary Fig. 23 and Fig. 6), seasonality, (TPV is active year-round, while PV develops in winter and disappears in spring, Fig. 7), dynamics, structures, and impacts

on weather³⁴. In particular, as discussed further, varying in strength, size, and position, PV influences the SPNA winter surface cooling. Since the range of PV migrations can exceed its diameter (Fig. 6), this influence needs to be assessed over the North Atlantic alone. The North Atlantic (Stratospheric) PV index (see the “Methods” section) meets this request and is compared in Fig. 5e, f with the other winter atmospheric forcing variables.

Why did convection continue to deepen after 2015 (the year of the highest winter cooling in the 1994–2023 period)?

It used to be expected that Labrador Sea convection would shoal immediately after an extreme forcing year, following a reduction in winter cooling, but is it always the case? Apparently, it is not, and to see why we are going to dissect all winter mixing events of the Argo era, examining them all year by year.

The deep CLS temperature, salinity, and density *observations* (*dots* in Fig. 4, while the *background gray lines* connect annual values) show very little scatter revealing the depth-selectivity of all 2002–2023 convective events. In particular, convection reached 1000 m extensively in 15 and marginally in two more cases, totaling about 77% of all 22 cases, while 500 m deeper, at 1500 m, the number of annual convective spikes drops to eight, or about 36% of 22. Seven of the eight cases with 1500 m and deeper convections occurred in straight 9 years spanning 2014–2022, while only one (2008³⁵) occurred in the other 13 years (2002–2013 and 2023), emphasizing the significance of the recent convective development to the ocean ventilation, circulation, and climate. The development was preceded by a record-warm shallow-convection state in 2010. The subsequent negative temperature, positive density, and positive convection-depth trends lasted for eight years, 2011–2018 (Figs. 3 and 4; 2011 preceded most trends, therefore included in the range). Such persistence of multiyear deepening of convection had a twofold effect on the mixed layer. Recurring convection incrementally cooled, densified, homogenized, deepened, and expanded the layer. In addition, the mixed layer, expanding with each event, was becoming increasingly susceptible to retaining weaker stratification (reduced density gradients) for longer, facilitating, as a result, future deepening of convection. This progressing development was initiated by the increasing NAO and WSHL early in the period (Figs. 4 and 5). Both NAO and WSHL reached their long-term highs in 2015. However, convection continued to deepen in significantly warmer winters, especially, in 2018's, afterward.

In 2015, WSHL reached the highest point of the entire 1994–2023 period, and then significantly reduced, which explains the deepening of convection only until 2015. The last three, 2016–2018, convections of the whole recent, 2011–2018, sequence of progressively deepening convections, demonstrated, for the first time, that the water column is capable of facilitating and extending deep mixing under weakening atmospheric forcing (e.g., NAO and WSHL) by accumulating and utilizing the residual effects of the previous cooling and mixing events on the density stratification. Retaining low-temperature high-density weak-stratification states imposed by past convections makes the water column susceptible to deeper convection in a year with comparable or reduced WSHL. Sustaining reduced vertical stability by retaining past mixed layer characteristics is the essence of *convective preconditioning*⁸, henceforth, *preconditioning*. As shown below, preconditioning is capable of overcompensating for reduced surface cooling facilitating recurrent convective deepening.

The deepening of convection continued through 2016–2018, the years with moderately cold winters, is the first observed case when preconditioning was a decisive factor for convective development. The 2012 and 2014–2017 residual annual cooling and densification (Fig. 4, 1000 m θ and σ) contributed to this preconditioning. Convection deepened in these years, with each winter mixing event leaving temperature lower and density higher than could be compensated by the post-convective temperature increase and density decrease, respectively. Consequently, the deep mixed layer was colder/denser in the next fall than in the prior one. The resulting residual temperature/density decreases/increases reduced the temperature/density barriers underlying the winter mixed layer, weakening the sub-surface stratification and preconditioning the sea for the subsequent

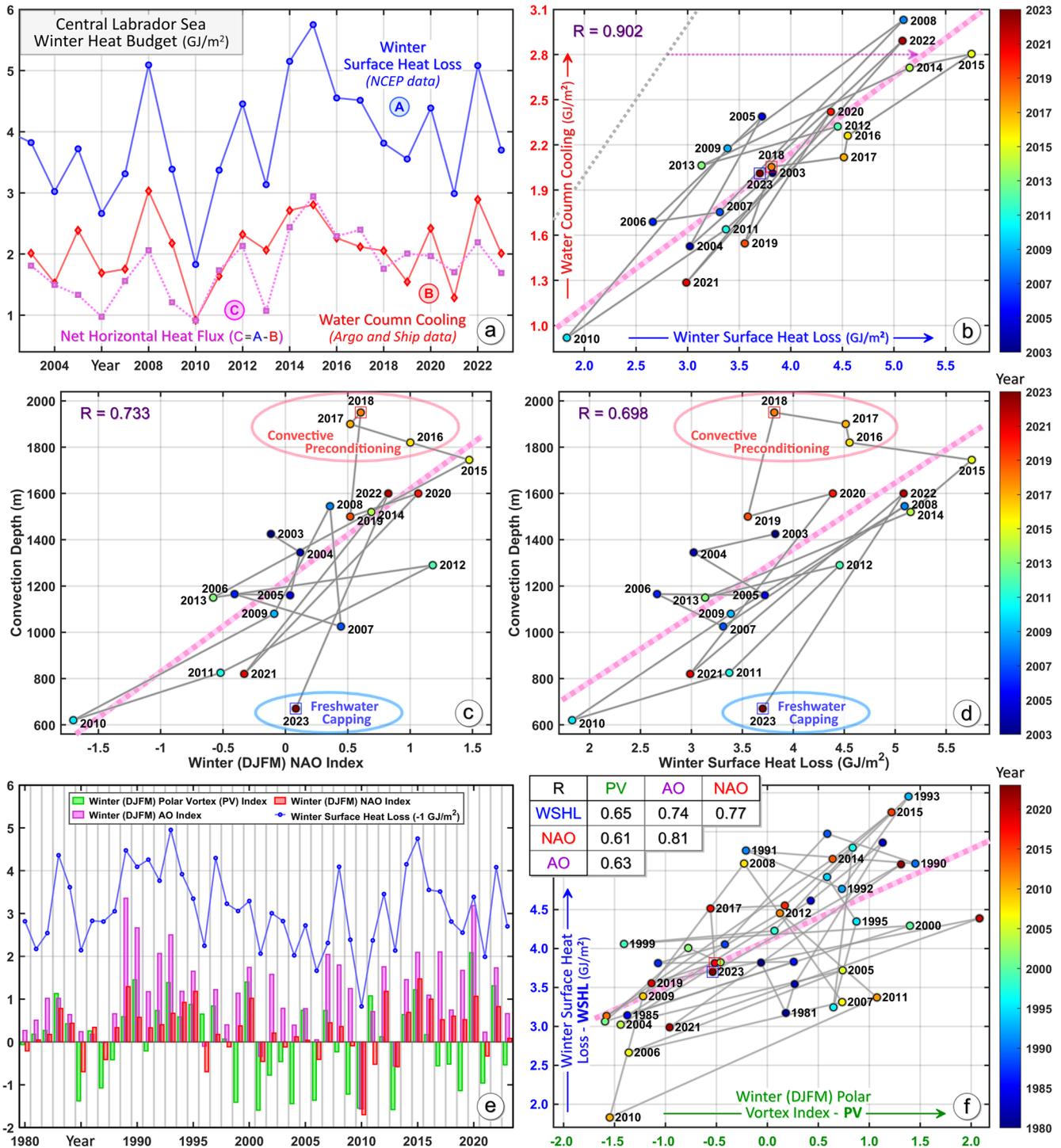


Fig. 5 | How do the Labrador Sea heat content and convection depth respond to the winter atmospheric forcing? **a** The (winter) surface heat loss (WSHL) (blue) and 15–2000 m layer heat content reduction (red) computed over the individually defined respective (surface and 15–2000 m layer) cooling periods; and their difference corresponding to the horizontal heat flux (light purple). The horizontal heat flux is generally higher in the years with increased WSHL. **b** 2003–2023 year-color-coded

scatter of the 15–2000 m layer heat content reduction versus WSHL. The linear fit line (thick pink) diverges from the equal-value line (gray) supporting the statement that the horizontal heat flux (e.g., thin pink dotted arrowed line) increases with the ocean cooling. Year-color-coded scatters of the convection depth versus the winter NAO index (c) and WSHL (d). The subpolar winter indices (e), the scatter of WSHL versus the winter polar vortex index (f).

convective seasons, reducing WSHL required to overcome the stratification barrier in each case in order for convection to reach deeper.

The years, 2016–2018, when preconditioning contributed to the deepening of convection stand out in the convection depths versus NAO and WSHL diagrams (Fig. 5c, d). 2018, being the farthest up from the Depth–WSHL regression line, showcases the largest impact of

preconditioning on convection, supporting and strengthening the hypothesis of preconditioning-driven facilitation of convection⁸. 2016–2018 had lower WSHL than 2015. Furthermore, 2015’s WSHL was the highest for the 1994–2023 period, while 2018’s WSHL was the lowest for the 2014–2018 period. However, despite the switchover in winter cooling, the deepening of winter convection continued for 3 more years after 2015, resulting in the

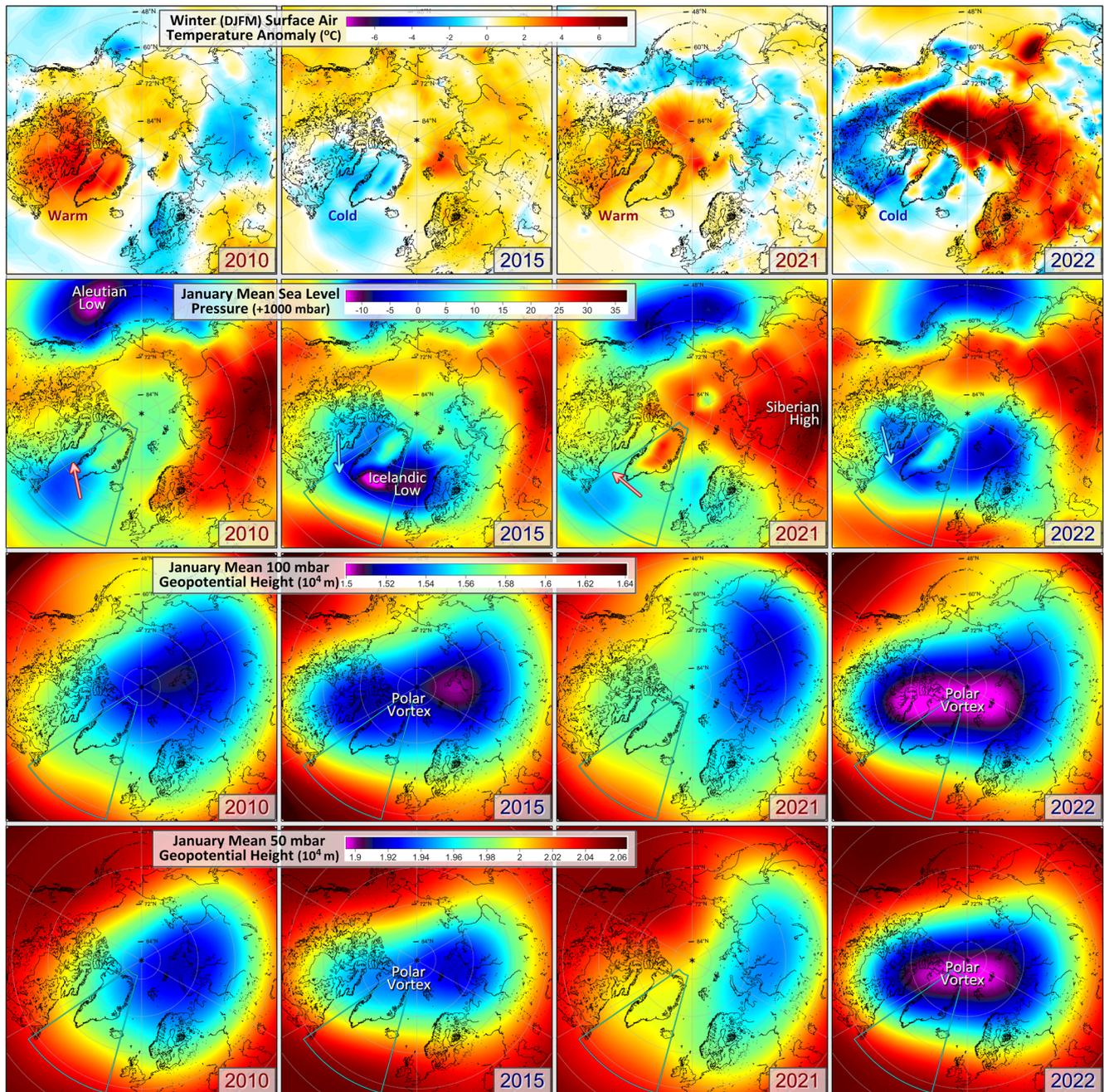


Fig. 6 | Weak (2010 and 2021) and strong (2015 and 2022) Labrador Sea atmospheric forcing conditions associated with changes in the tropospheric and stratospheric circulation. 2010, 2015, 2021, and 2022 winter (DJFM) mean air temperature anomalies (°C), January sea level pressure, and January 100 and

50 mbar geopotential surface height (source: NCEP/NCAR Reanalysis; region: polar-subpolar Northern Hemisphere; baseline climatology: 1991–2020 mean seasonal cycles). The trapezoid represents the zonal averaging domain.

development of the most significant, in terms of volume, depth, and density, class of LSW since the mid-1990s.

What inhibited and reversed the development of deep convection in the Labrador Sea that started in 2012 and progressed through 2018?

In 2019 and 2021, WSHL were the lowest since 2013, making winter convection shallower and the sea warmer than in the previous years. In 2020 and 2022, however, while both NAO and WSHL increased significantly, surpassing the 2018 values, convection was ~350 m shallower than in 2018. In 2019 and 2023, WSHL were comparable, but convection was ~800 m shallower in 2023. Such disparity in the responses to WSHL is explained by reduced preconditioning after 2018, and rapid freshening in 2023 making

restratification (meaning restoration or buildup of water-column stratification) another key factor, along with WSHL and preconditioning, controlling winter convection in the Labrador Sea. Preconditioning and restratification affect convection in opposite ways, enhancing or reducing the action of WSHL.

The persistent deepening of convection during 2014–2017 progressively cooled, densified, and homogenized the intermediate layer to the point when below-normal WSHL of 2018 gave the deepest convection since the mid-1990s. In 2020 and 2022, on the contrary, winter convection was comparably inhibited due to the lack of sufficient preconditioning of the intermediate layer. Indeed, the reduced WSHL, shoaled convection, and uncompensated losses of cold dense LSW_{2012–2018}, enhanced by the accumulation of warmer fresher less-

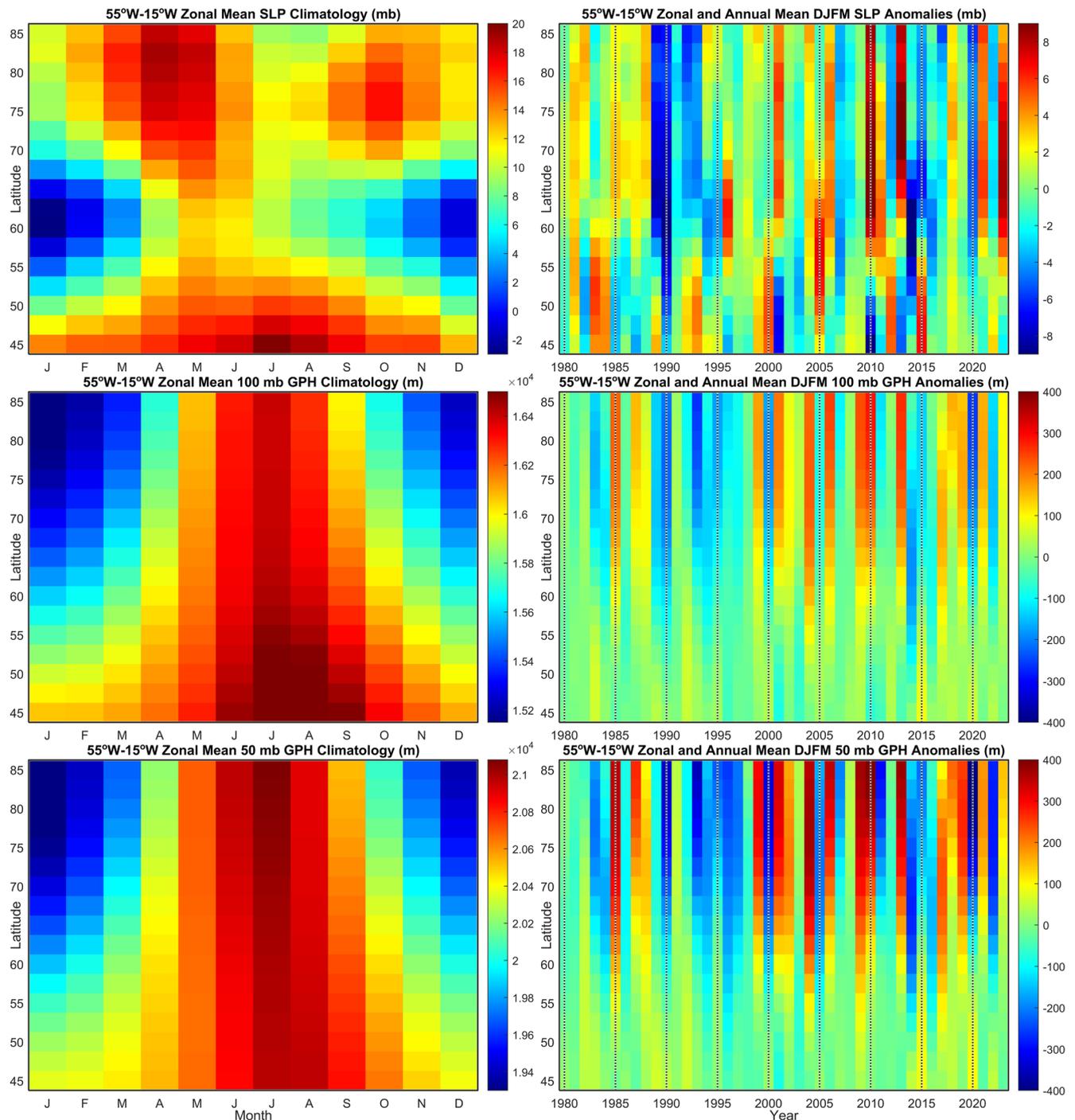


Fig. 7 | Zonally averaged sea level pressure, and 100 and 50 mbar geopotential surface height climatology and anomalies. 1981–2010 monthly climatologies (*left*) and winter (DJFM) mean anomalies (*right*) of the 55°W–15°W zonally averaged

mean sea level pressure (SLP, *upper*), 100 mbar geopotential height (GPH, *middle*), and 50 mbar GPH (*lower*).

dense water in the upper 800 m, in 2019 and, especially, in 2021 and 2023, made the moderately deep convections of 2020 and 2022 unable to reverse or even slow the recent (2019–2023) winter mixing shoaling and intermediate layer warming trends.

2023, being the farthest away below the Depth–WSHL and Depth–NAO regression lines (Fig. 5c, d), showcases the most recent game change in the history of Labrador Sea convection, possibly similar to the shutdown of convection that happened during the Great Salinity Anomaly in the late 1960s–early 1970s, when a strong ocean freshening inhibited deep convection¹. The recent (2019–2023) freshening trend mapped against the other sea-state and atmospheric-forcing metrics, allows us to assess and

predict the degree to which a rapid restratification can suppress an expected outcome of moderately strong winter surface cooling. The capping effect of a rapid freshwater buildup in the upper layer may bring an endured shutdown of convection¹, which has probably already started with the 2023 freshening event.

Overall, being about 800 m deep in 2021 and shallower than 700 m in 2023, thus making half or less the depths of the previous year (2020 and 2022, respectively) convections, the 2021 and 2023 winter convections were the shallowest since 2011, and among the four shallowest convections since the mid-1980s. Also, the 2021 and 2023 recoveries of the intermediate layer from the post-convective low-stratified cold dense states of the previous

years were among the fastest observed, making it the warmest and least dense since 2014.

How long does it take for convective signals to reach the boundary current?

Other than the factors determining the strength and depth of convection, an important aspect of the process is the rate and amount of modification or transformation, with which the signals originating in CLS are resulting to the boundary regions. As a first step in this direction, I use the longest Labrador Sea mooring record to track all CLS signals from the mid-1980s onward to the western boundary of the deep basin.

The Hamilton Bank mooring is located around the 1000 m isobath on the upper Labrador Slope (ULS), in the mainstream of the Deep Labrador Current. The quality-controlled calibrated 36-year-long 48-h (Fig. 4, *translucent light brown dots*), monthly (*dark brown line*) and yearly (*gray line*) low-pass filtered (based on adaptive filter design) near-bottom temperature measurements (Fig. 4) raise two important aspects of the interannual and seasonal connectivity between the ULS, CLS and Subpolar Gyre as a whole.

The interannual ULS near-bottom (1000 m) temperature changes were analyzed by comparing the monthly low-pass-filtered annual cold and warm states (*dark brown line*), and the yearly low-pass-filtered values (*gray line*) with the NAO, WSHL, and CLS temperature series. The ULS annual cold and yearly low-pass states are correlated with the named atmospheric winter forcing variables, and closely follow, even mimic, the corresponding CLS 1000-m-depth temperature changes. The likeness of the ULS and CLS temperature records can be explained by the similarity of the mixed-layer temperature, density, and depth (Figs. 1c–e, 2–4 and Supplementary Figs. 6–8) and annual pycnostad spatial extent changes (e.g., Fig. 8 in ref. 7) changes. The changes in convection may, therefore, directly control the amount and properties of the waters entrained by the boundary flow both locally and remotely, e.g., via the spreading of LSW to the Irminger Sea^{10,11}. The changes imposed by winter convection on seawater properties, pycnostad geometry, and steric height, either directly or while spreading away from the source, affect the subpolar circulation and associated heat fluxes shaping the boundary current properties in the Labrador Sea.

The ULS near-bottom temperature series features a strong seasonal cycle throughout the record. Unlike the CLS 1000-m-depth temperature series, it shows no apparent dependence on the strength of winter atmospheric forcing and convection in CLS. Furthermore, its range or double-amplitude, ~ 0.5 °C on average, significantly exceeds the magnitude of the CLS seasonal changes at the respective depth (1000 m) in all years. This means that the Deep Labrador Current seasonality is not directly driven and controlled by winter convection. Its possible causes include seasonal changes in the shelf-slope and slope-interior exchanges, transports, entrainment, and mixing.

Even though there is no conclusive evidence to explain why the interannual signals transferred from CLS to ULS remain largely unmodified, while the CLS and ULS seasonal cycles are so much different, one fact points at the source region of both phenomena. The similarity of both interannual and seasonal near-bottom temperature changes at the ULS (Hamilton Bank in Fig. 4) and upper Greenland Slope³⁶ locations suggests that both interannual CLS and seasonally-imposed signals are likely acquired by the boundary current anywhere between the eastern Labrador Sea and the Irminger Sea.

What caused the convective shutdown of 2021?

When discussing the extreme winter mixing and water column conditions registered in CLS in 2021, I stated that those came as a direct response of the sea to an anomalously weak winter surface cooling. Here and in Supplementary Note 7, we advance our understanding of this and other anomalous CLS states by showing how WSHL responded to changes in atmospheric dynamics.

The 2021 WSHL that was the lowest for the 2014–2023 period sharply contrasts with the 2015 WSHL that was the highest for the whole 1994–2023

period (Figs. 4, 5 and 8). The 2021 Dec–Mar NAO (Figs. 4 and 5c, e, f) and AO (Fig. 5e, f) indices were also the lowest for the 2014–2023 period. Often, but not always, the lower winter NAO states bring weaker subpolar zonal winds, i.e., westerlies, higher air temperature anomalies (ATA), and, consequently, lower WSHL (Figs. 4–6). Also, the meridional sea level pressure (SLP) gradient, NAO, and AO changes are interrelated (Supplementary Note 7, Figs. 5–7 and Supplementary Figs. 24–26). However, the NAO index is not solely and fully reflective of the circumpolar atmospheric dynamics, governing the regional air–sea interactions, particularly, WSHL responsible for wintertime water-column cooling and convection (Figs. 5–7). Figure 6 explains why some extreme atmospheric forcing situations require a deeper understanding of the three-dimensional atmospheric dynamics based on several state variables, combined with the NAO index. The four situations presented in Fig. 6 raised a new approach to both analysis and interpretation of the multilevel atmospheric data. The choice of two winters for each of low and high surface cooling situations was guided by the WSHL ranking (Fig. 5a). To gain understanding what was causing or enhancing these atmospheric-situation switchovers, the respective ATA, SLP, 100 mbar geopotential height (GPH), representing tropopause-to-low-stratospheric PV, and 50 mbar GPH, showcasing PV, and fields are compared in Fig. 6.

The similarity of the warm and cold “blobs” in the ATA maps suggests similar, possibly reversed, signal spreading. Indeed, in the 2010 and 2021 January SLP maps, the low-pressure systems, associated with the Icelandic Low (IL), are reduced in size and shifted south-to-southwest, while in 2015 and 2022, the respective low-pressure systems deepened, increased in size, and shifted northeast. The arrows schematically show the average surface wind direction. The weaker southerly-displaced low-pressure systems bring more air from the east, while the stronger northeasterly-displaced systems intensify the westerly-to-northerly winds bringing cold dry winter air from Eastern Canada and the Arctic. In January of 2021, the Polar Vortex shows as strongly weakened and collapsed with its center being shifted toward Siberia, making the Labrador Sea winter anomalously mild (Fig. 6). The diminished-to-reversed westerlies, increased ATA, and consequently reduced WSHL led to much shallower convection in 2021 than in the previous ten winters, making the whole intermediate layer, particularly, its deeper half, warmer and less dense than in the previous six years.

The PV–IL interaction can also be diagnosed, and its strength assessed following simple hydrostatic or air mass distribution considerations. The PV regime changes correlate with the IL SLP changes. Indeed, in both climatological fields (Supplementary Fig. 23) and most of the monthly (e.g., 2015, 2022 in Fig. 6) to instantaneous atmospheric situations with a strong undisturbed PV, the high-gradient 50 and 100 mbar GPH zones pass over IL, largely overlapping with the latter. When the PV-linked stratospheric low, even partially, overlays IL, it amplifies the air mass reduction toward the IL center, consequently lowering SLP there, and, as a result, increasing the NAO index.

By contrast, a weakened, disrupted, or collapsed PV flattens the hosting geopotential surfaces, usually relocating or scattering their lows northwardly-to-eastwardly of IL (e.g., 2010 and, especially, 2021 in Fig. 6). By distancing itself from IL, PV increases the weight of air mass and SLP in IL, thus lowering the NAO index.

To investigate the hydrostatic adjustment and synergy of PV and IL, the 55°W–15°W monthly zonal mean SLP, 100 mbar GPH and 50 mbar GPH and their anomalies were computed for each latitude from 45°N to 85°N (Fig. 7, left, Supplementary Fig. 24) and averaged over Dec–Mar periods (Fig. 7, right, Supplementary Fig. 25). Supplementary Note 7 provides further explanation of the new metrics, including the North Atlantic PV, henceforth, PV index, their design and meaning. It is only noted here that the meridional 50 mbar GPH patterns, especially those containing positive anomalies and gradients, which are mainly associated with PV disruptions and collapses in the North Atlantic, overlay similar but shorter-span (45°N–60°N) patterns in SLP. As a measure of this likeness, the PV index, obtained for all winters as the inverse meridional gradient of the 50°W-to-25°W zonally averaged 50 mbar GPH (Supplementary Note 7), was correlated with the other atmospheric forcing metrics. These results

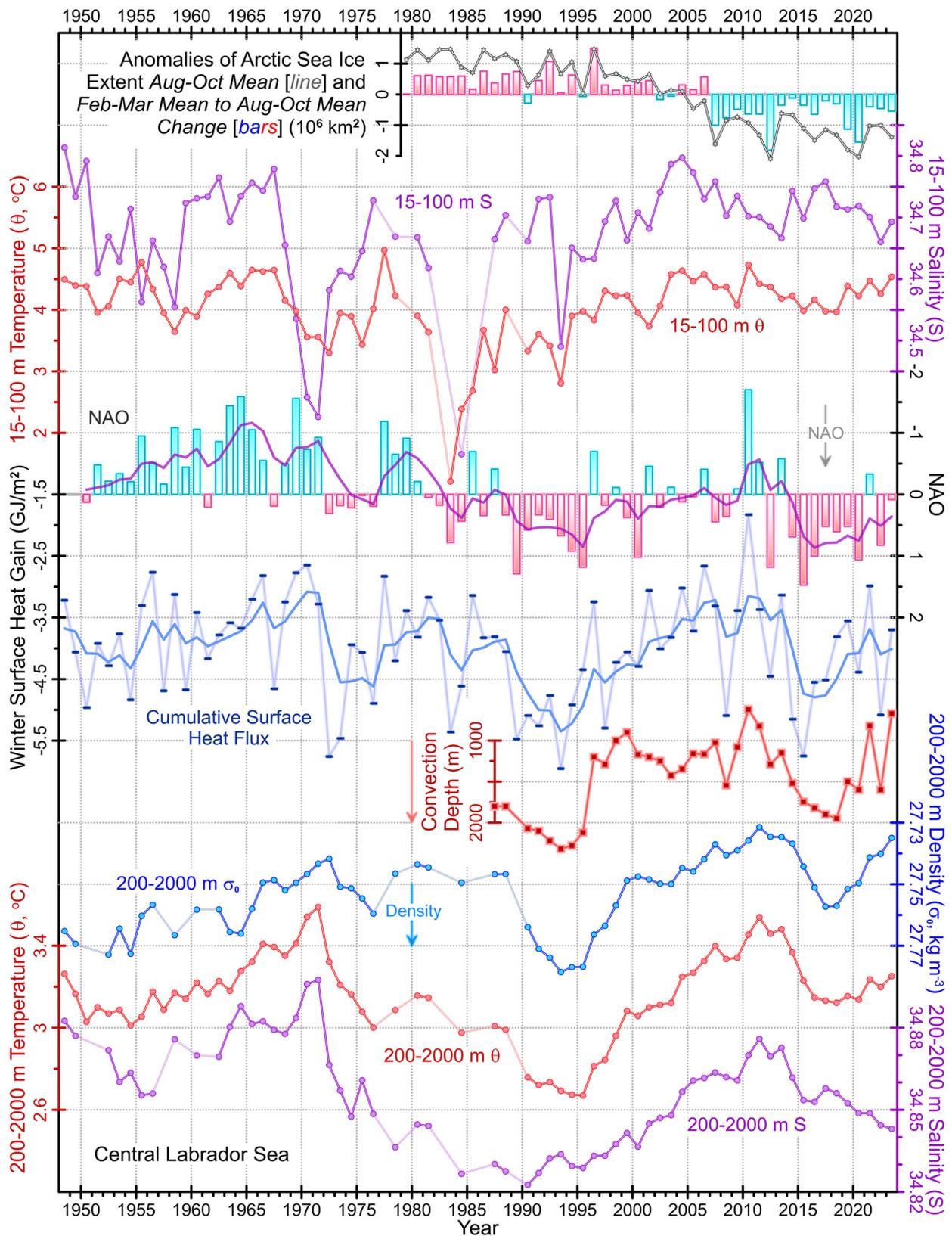


Fig. 8 | Time series of annual ocean state, atmospheric forcing, and Arctic sea ice extent. *Top-down:* The Aug-Oct Arctic sea ice extent, and Feb-Mar to Aug-Oct change anomalies; the central Labrador Sea (CLS) 15–100 m vertically and annually averaged de-seasoned salinity (S) and temperature (θ); the winter NAO index (*inverted*); the CLS surface heat flux integrated over individually defined cooling seasons (*blue*); the low-pass left-side-window filtered NAO and surface heat flux (*solid lines*); the convection depth; the CLS 200–2000 m vertically and annually averaged density (σ_0 , referenced to 0 dbar), θ and S.

quantitatively support my statement that spatially aligned PV and IL are likely to make each other stronger, NAO more positive, westerlies more intense, and WSHL higher.

Bound with the climatological IL and Azores High, the NAO index is highly correlated with the AO index, which in turn is bound with the tropospheric polar vortex maintained by the Icelandic and Aleutian Lows (Fig. 5 and Supplementary Fig. 26). In support of the noted dynamical link between PV and IL, there is a significant statistical relationship (above-critical correlation) between these two indices, WSHL and the PV index.

Summarizing the aforesaid, as PV intensifies, and reduces in size, while a large part of it overlaps IL, it makes IL deeper and bigger, thus increasing the NAO index and speeding up the zonal airflow. The resulting coaction of PV and IL intensifies the westerly-to-northerly winds over the Labrador Sea, strengthening the atmospheric forcing, and increasing WSHL. Another consequence of this situation is an increased transport of cold continental and Arctic air to the whole subpolar North Atlantic. By contrast, as PV weakens, disrupts, and spreads out, it distances itself from IL, reducing or even fully terminating their overlap. The weakening and shift of PV makes IL weaker (less depressed) and smaller. With PV and IL located far from each other, the zonal flow is less stable and more disrupted, making the NAO index, surface forcing, and WSHL low.

What caused the convective shutdown of 2023?

Considering that both 2020 and 2022 had moderately strong convections, the shoaling of winter convection in 2023 to less than half of the previous convection depth enhanced the rapid decline in winter mixing that occurred two years earlier. In 2023, the depth of winter convection reduced to a record low, and the respective pycnostad thinned with its σ_1 density being pushed to the low end of the historic LSW σ_1 range (Fig. 3). The 2021 and 2023 shutdowns of deep convection had similar features, including low pycnostad densities and substantial pycnostad thinning in April. Furthermore, similarly to 2021, a PV collapse did also occur in the winter of 2023, making the average meridional gradients of the 50 and 100 mbar GPH weak, and their anomalies positive (Fig. 7). However, despite the similarities in appearances and associated atmospheric regimes, the leading causes of the 2021 and 2023 convective shutdowns were different. The difference was already obvious in the results we discussed earlier. First, according to Figs. 2 and 3, 2023 had a much colder and fresher mixed layer than 2021. Then, Fig. 4 and especially Fig. 5c, d showed us that the shoaling of convection in 2023 did not follow the suit of a typical moderately cold winter. Indeed, the convection of 2023 happened to be much shallower than we would expect from the magnitude of winter surface cooling. Furthermore, 2018 and 2023 had similar surface cooling situations with low-to-moderate WSHL. Both of these years are indicated by squares in Fig. 5b–d. As seen in the scatter plots emphasizing the principal difference between these years, in 2018, convection was much deeper than prescribed by surface cooling alone. Moreover, the winter convection of 2018 was the deepest since 1995, and the reason why it exceeded the expected depth by ~ 700 m is the convective preconditioning that I explained earlier. In 2023, by contrast, the strength and depth of winter mixing were much reduced, giving one of the shallowest convections on record, which was ~ 600 m shallower than we would expect it to be under the same surface cooling, but average stratification conditions. The observations shown in Figs. 2, 3, 8–10 point at the sea-wide freshening rapidly progressing and deepening since 2021 as the main cause of the 2023 convective shutdown.

In 2023, the Labrador Sea was the freshest throughout all depths from 300 m (or shallower) to 700 m, most certainly, since 2002 (Fig. 3) and probably since the early 1980s (Fig. 10). To track the present arrival and future departure of this freshening event I suggest to use salinity averaged over the 300–700 m layer of CLS (Fig. 9). This choice is dictated by the following consideration. With the typical annual convection depths exceeding 700 m (Fig. 4), the CLS 300–700 m layer is mostly mixed, homogenized, and ventilated every winter (Fig. 3). This layer retains upper-ocean signals in cases of shallow convection. The 300–700 m layer mean salinities (Supplementary Fig. 18) averaged over the post-convective

April–December periods (Fig. 9, the seasonal cycle was removed prior to averaging) follow the 2017–2023 monotonic freshening trend to a record fresh state in 2023.

What made the upper Labrador Sea so extremely fresh in 2023?

Here, I will present the evidence that the freshening of the Labrador Sea that reached its record point in 2023 was probably caused by the anomalously high Arctic sea ice losses of recent years, enhanced by the freshwater release from the Beaufort Gyre (BG) that started after 2017 when its freshwater content was the largest on record.

The Arctic sea ice extent and volume anomalies (ASIEVA), freshwater content, and outflow changes are usually viewed in light of the BG regime shifts, which result in transitions between freshwater accumulation, retention, and release^{37–41}. In particular, the recent stabilization of the BG freshwater content was argued to signal the beginning of a huge freshwater release⁴⁰. Once occurred, this release would boost the Arctic freshwater outflow flux ultimately inhibiting, if not shutting down, CLS convection. However, it might take a decade for the BG-sourced freshwater (BGFW) to fully arrive in CLS⁴¹, while the 2023 *freshwater-driven* convective shutdown occurred sooner than that. To explain the 2023 shutdown, I hypothesize that when cooccurring with a BGFW release, an anomalously high sea ice melt/loss/retreat may boost Arctic freshwater export faster, and to a larger degree, than the BGFW release alone. This implies that in both BGFW stabilization/retention and release states, a negative winter-to-summer ASIEVA change (i.e., an increased sea ice melt) reduces surface salinity, consequently increasing freshwater export, and, as a result, reducing salinity at all destination locations, including CLS.

Figures 8 and 9 include the late-summer (August–October-mean) ASIEVA (*line*) and late-winter (February–March-mean) to late-summer (August–October-mean) ASIEVA change (*bars*, change is opposite in sign to loss) series. Figure 9 also includes two BG time series that I constructed from the Beaufort Gyre Exploration Project datasets: the BGFW content gridded data were spatially averaged for each year of the 2003–2022 period; the McLane Moored Profiler measurements from four BG locations⁴² were processed to obtain a continuous BG upper-layer (60–80 m) salinity record as documented and shown in Supplementary Note 7 and Supplementary Figs. 27–29.

The late-summer ASIEVA and winter-to-summer ASIEVA changes were particularly low (i.e., high absolute magnitudes) in 2007, 2012, 2019, and 2020 (Fig. 9). Furthermore, during the entire 2007–2012 period, the winter-to-summer ASIEVA changes surpassed -0.5×10^6 km² (extent) and, mainly, -1×10^3 km³ (volume). From 2003 to 2016, BGFW closely followed the major ASIEVA changes and trends. However, over the following period (2016–2022), BGFW first stabilized, then declined, while the seasonal and annual sea ice losses increased over the first half of this period. Specifically, the 2019 and 2020 winter-to-summer ASIEVA reductions were third and second (for extent), and fourth and third (for volume) record highs, respectively. The meltwater anomaly formed in these two consecutive years cooccurred with the beginning of the ongoing BGFW release, synergizing the effects that may be registered in the Labrador Sea salinity series.

BG 60–80 m layer average salinity responded to the largest single-year sea ice retreat that occurred in 2007, with the steepest and largest decrease to the salinity minimum (Fig. 9). Salinity started to increase immediately after reaching its record low point. It continued to increase until 2013, stabilized for a short period, and in 2015, it started to decrease again. The sustained freshening of the 60–80 m layer of BG going on from 2015 to 2019 generally coincided with the progressive sea ice retreat of 2015–2020.

The ASIEVA, BGFW content, and BG 60–80 m layer salinity signals that we just discussed correlate with the changes in the Arctic freshwater content. These changes directly affect the freshwater flux passing through the Arctic–Subarctic gateway, affecting Labrador Sea salinity and hence convection. We will now connect the Arctic freshwater signals with the changes in Labrador Sea salinity.

The de-seasoned, and vertically and annually averaged CLS 15–100 m salinities reached their recent lows in 2013 and 2022 (Figs. 8 and 9). The

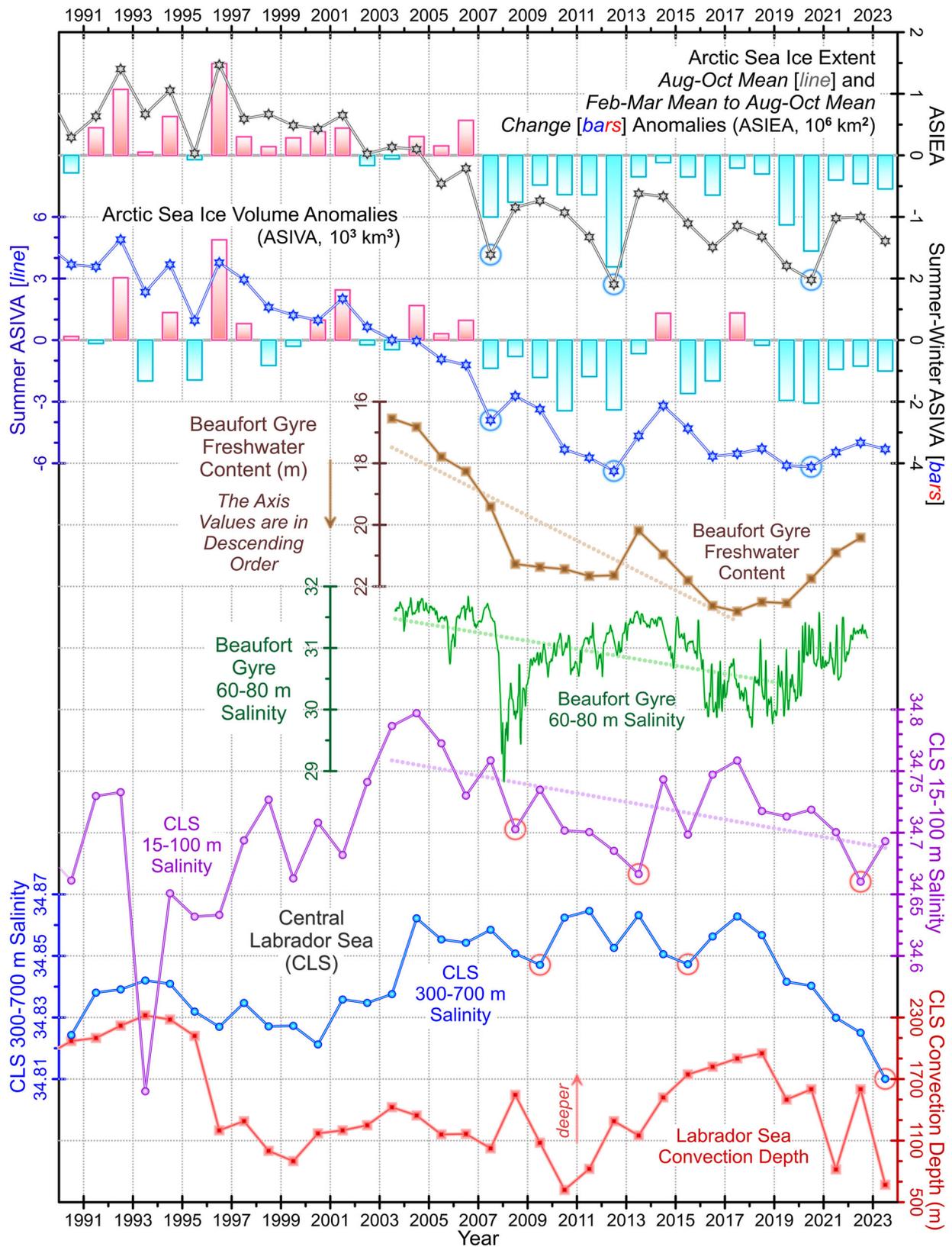


Fig. 9 | How long does it take for the Arctic freshwater release anomalies to enter the Labrador Sea? *Top-down:* The Aug–Oct Arctic sea ice extent and volume, and respective Feb–Mar to Aug–Oct change anomalies; the Beaufort Gyre freshwater content (m) and 60–80 m layer average salinity series based on the ship-based and McLane Moored Profiler measurements, respectively, collected as part of the

Beaufort Gyre Exploration Project; the de-seasoned and averaged, first vertically over the 15–100 m layer, and then annually, central Labrador Sea (CLS) salinity, and the de-seasoned and averaged, first vertically over the 300–700 m layer, and then over the Apr–Dec period CLS salinity; the CLS convection depth.

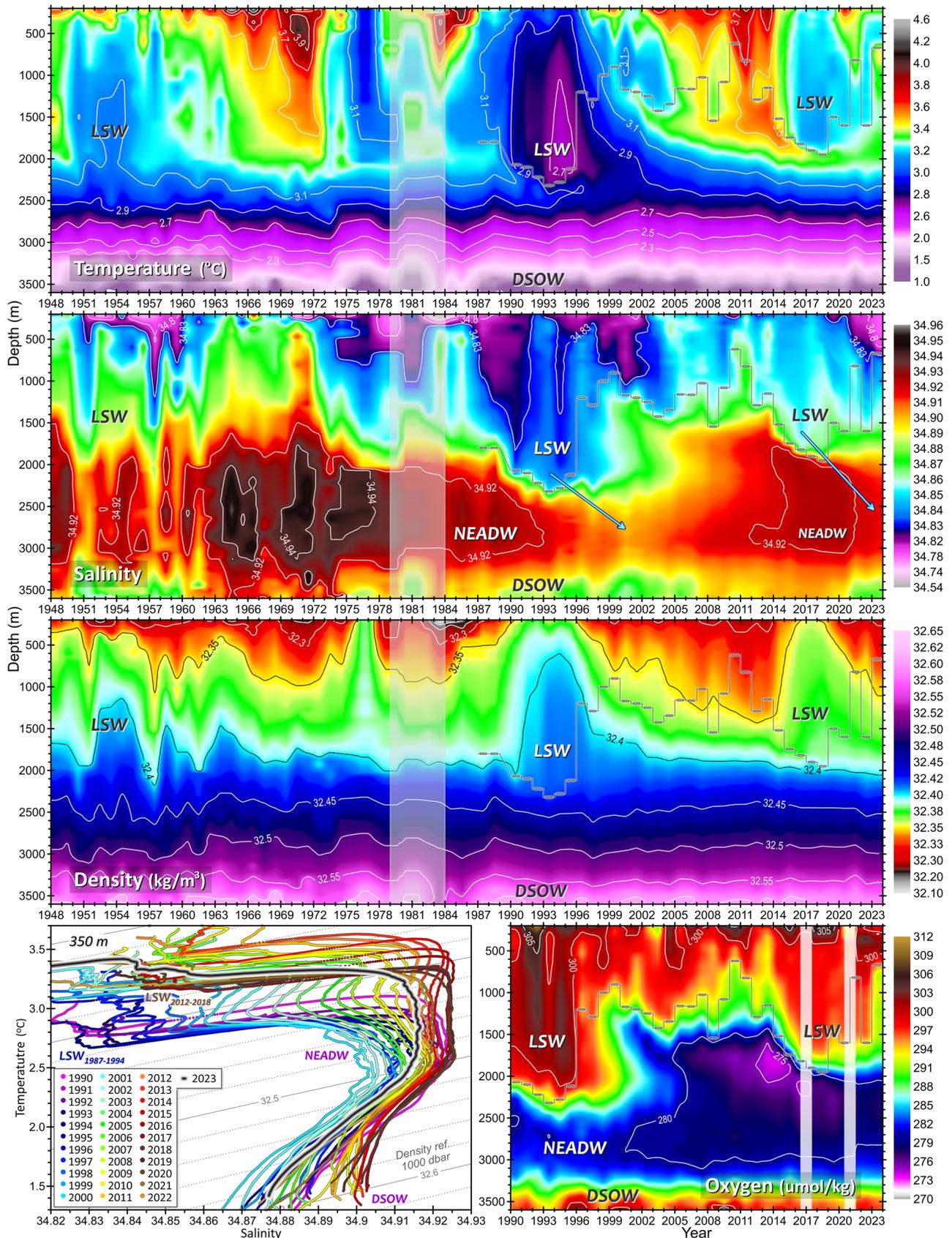


Fig. 10 | Convective cycles dominate decadal water property changes in the Labrador Sea. *Top-down:* The 1948–2023 central Labrador Sea annual temperature, salinity, and density (1000 dbar pressure referenced) profiles based on the edited and calibrated ship (except for 2017 and 2021) and 2017 and 2021 float observations; the 1990–2023 annual temperature–salinity curves; and dissolved oxygen profiles.

LSW, NEADW, and DSOW indicate Labrador Sea Water, Northeast Atlantic Deep Water, and Denmark Strait Overflow Water, respectively. Horizontal lines indicate the convection depths computed for the period of sufficient hydrographic observations (1987–2023).

entire 200–2000 m layer was affected by progressive freshening events of 2008–2009, 2014–2016, and 2019–2023 (Figs. 2 and 8). The largest CLS freshening event of the past 37 years (1987–2023) was presently (2023) registered in the 300–700 m layer (Figs. 9 and 10). Whether the low-salinity point of 2023 was a culmination or a continuation of the 2017-to-2023 monotonic freshening trend will be seen in the near future. Nevertheless, the recent freshening trend makes a substantial difference in our comprehension of the signal exchange between the Arctic and North Atlantic. Even though the 2008–2009 and 2013–2014 CLS freshening events resembled in their timing, lagged by 1–2 years, and in their appearance the 2007 and 2012 negative ASIEVA, one might still doubt if the two sequences of events were really connected. But the recent, and possibly still ongoing, freshening of the Labrador Sea proves that all three mentioned CLS freshening events were caused by the discussed Arctic freshwater regime changes. Furthermore, given the recent changes in ASIEVA and BGFW content, there is a strong possibility that the CLS freshening trend may continue inhibiting CLS convection for longer.

The 2012–2023 convective cycle and 2012–2018 class of Labrador Sea Water in the context of long-term water-mass production and property changes

Having a full picture of the recent convective development and its decline as well as the causes of both, we will now compare the whole convective cycle with those observed in the past. Given that the LSW class developed between the late 1980s and the mid-1990s was the largest, coldest, and densest ever documented, we will make notes of its similarity with the LSW class discussed in this study.

Temporal evolutions of the *annually averaged full-depth CLS oceanographic profiles* are shown in Fig. 10. Here, the merged temperature, salinity, and σ_1 (density referenced to the 1000 dbar pressure level) observations span the period of 1948–2023, while the dissolved oxygen profiles are presented only for 1990–2023 when high-quality oxygen measurements with sufficient vertical resolution became available (see the “Methods” section). Furthermore, the 2017 and 2021 temperature, salinity, and σ_1 profiles are entirely Argo-based as ship-based measurements were unavailable these years. The annual CLS profiles presented here for all other years are ship-based.

Large decadal-scale temperature, salinity, and σ_1 anomalies dominate the intermediate layer of the Labrador Sea (Figs. 8 and 10). The most significant or *major multiyear cooling freshening events* were initiated and shaped by recurrently intensifying and deepening winter convection. In particular, the three such events registered in the past 76 years had the convective cooling freshening reaching deeper than 2000 m. Their temperature and salinity lows were reached in the mid-1950s, early-to-mid-1990s, and late 2010s. Being imposed by shorter and shallower convective developments, the *minor cooling freshening events* of 1974–1978 and 2000–2003 did not affect the decadal trends as much as the major ones. The three major cooling events were separated by periods of *mid-depth warming and salinizing*. Record first and second temperature highs were reached in the early 1970s and early 2010s, respectively.

The intermediate (200–2000 m) layer is dominated by locally formed cold fresh dense LSW. Therefore, each new multiyear convective cycle startup, as well as each of its phase changes, e.g., from intensification and deepening to relaxation and shoaling, reverses long-term trends of water-column or vertical-layer variables. The mid-1980s-to-mid-1990s development of a record cold fresh dense gas-rich state of the intermediate layer illustrates this connection. Recurrently formed progressively cooling, densifying, deepening, and expanding LSW determined the intermediate layer and whole water-column trends spanning the mentioned period. The duration, persistence, and strength of winter convection during this phase led to major changes in the entire water column of the Labrador Sea, filling its 200–2500 m layer with record cold dense deep LSW, and affecting its overall heat, freshwater and gas (e.g., dissolved oxygen) content (Fig. 10), steric height and sea level⁵. The major Labrador Sea convective cooling event

was followed by a period of warming, 1995–2010, occasionally interrupted by short-lived bursts of moderately deep convection (e.g., 2000–2003, 2008).

In 2012 the sea again entered the 2012–2018 phase of progressively deepening convection. During these 7 years, the intermediate layer steadily cooled, densified, freshened, and became more gas-ventilated (Figs. 8 and 10), following suit of the 1987–1995 convective development but in a warmer saltier less-dense sea. The 2019–2023 convective relaxation phase followed the intermediate layer warmed reaching its record high temperatures in 2021 and 2023, when winter convection was only 800 and 700 m deep, respectively, resembling the 2010 and 2011 convective shoaling and layer warming. The recent shutdown of deep convection and intermediate layer warming completed the third major Labrador Sea multiyear convective cycle since the 1940s. Similarly to the first two cycles, this cycle is likely to define the variability of seawater properties in the deep North Atlantic.

The 2012–2018 LSW class came as a second large, dense, and deep since the late 1950s. The annual temperature–salinity curves (Fig. 10) summarize the appearance of the two fully and thoroughly resolved LSW classes — LSW_{1987–1994} and LSW_{2012–2018}. The latter was warmer, saltier, and less dense than the former, nevertheless, both were comparably persistent in their development. Each class eventually formed a tight distinct cluster in the *T–S* diagram, providing a useful benchmark for North Atlantic circulation and water mass transformation studies.

Figure 8 summarizes the changes in oceanographic conditions imposed by the major convective cycles of the past 76 years on the intermediate layer of the Labrador Sea. There is an important difference between the upper and intermediate layer responses to the high-frequency and low-frequency WSHL variability. The upper (15–100 m) layer was record cold in 1983, warming afterwards for about two decades. From time to time, this layer showed a simultaneous response to a short-lived WSHL extreme, e.g., 1973, 1977, 1983, 1993, and 2010. The intermediate layer characteristics and convection depth, however, are not sensitive to the isolated NAO and WSHL extremes, showing a smoothed-lagged response to the atmospheric forcing. The reason for this discrepancy in the oceanic responses is the ability of the intermediate layer to carry forward its partial past states or preconditioning, analogously to convective preconditioning. This type of response can be simulated or mimicked by either recursive filtering or, as shown in Figs. 4 and 8, non-recursive low-pass filtering with a 5-year left-side triangular time window discussed earlier. Apparently, the convection depth and intermediate layer variables, especially temperature and density, closely follow the low-pass *left-side-window* filtered NAO and surface heat loss series (Figs. 4 and 8) signifying the role of convective preconditioning (simulated or mimicked by low-pass filtering) in shaping the deep-sea changes.

Has the recent convective signal been already transferred to the deeper water masses?

Other than Labrador Sea Water, Fig. 10 presents Northeast Atlantic Deep Water (NEADW) and Denmark Strait Overflow Water (DSOW). Both NEADW and DSOW originate from the cold fresh dense overflows from the Nordic Seas—the Iceland-Scotland and Denmark Strait Overflows, respectively, but the former undergoes a longer and more substantial mixing, transformation, and modification along its path than the latter¹⁹. The NEADW circulation is also affected by decadal LSW volume changes over or near its path²⁵. As a result, while the vertically uniform NEADW salinity trends span 2–3 decades each (e.g., 1975–2000 and 2000–2020, higher instrumental noise before 1975), DSOW, similarly to LSW, showcases strong variations on decadal and shorter time scales. The two recent NEADW salinity lows, occurring around 2000 and 2022 (or even 2023), have an elegant explanation¹⁹. The first low occurred 6–7 years after LSW came to its deepest freshest point in 1993–1994. The second low, similarly lagged the recent deep fresh LSW point by 6–7 years. This time lag is explained by a *two-stage/step/phase signal transfer*. First, LSW spreads to the Mid-Atlantic Ridge location, where it gets massively entrained by NEADW. This transfer takes about three years^{10,11}. Then, after being massively diluted and freshened by LSW west of the trenches of the Ridge, NEADW spreads underneath LSW back to

the Labrador Sea taking 3–4 years for this transfer¹⁹. The two transfers added together give us the sought LSW-to-NEADW time lag of at least six years. The evidence of continuous entrainment of LSW by the deeper waters in the Irminger and Iceland basins reconfirms that the contribution of the Labrador Sea to the AMOC is higher than recently suggested (e.g. ref. 27).

How did the oxygen content respond to the convective shutdown?

Annually averaged profiles of the CLS quality-controlled drift-corrected dissolved oxygen measurements show how convection affected the Labrador Sea oxygen content during 1990–2023 (Fig. 10). The 1987–1994 and 2012–2018 deepening convective developments produced large volumes of well-ventilated LSW actively supplying the deep North Atlantic with the atmospheric gases. The annual vertical extents of elevated oxygen concentrations follow these developments. The oxygen concentrations were record high during 1992–1994, providing a critical oxygen benchmark for the rest of the ocean.

The moderately deep convections of 2000–2003 also contributed to ocean ventilation, but, obviously, to a lesser degree than the other two convective developments, highlighting the relative significance of the 2012–2018 development to natural and anthropogenic gas exports. Even though convection substantially shoaled from 2000 m in 2018 to 800 m in 2021, moderately deep (1500–1600 m) convections of 2019, 2020, and 2022 kept the atmospheric gasses (e.g., dissolved oxygen, carbon dioxide, anthropogenic gases) supplied to the 0–1500 m layer, retaining, even increasing, their concentrations. The situation changed in 2023, when similarly to the other presented variables, oxygen responded to the second rapid shoaling of convection in three years. Namely, in 2023, the 600–1600 m layer average oxygen concentrations were the lowest for the 2014–2023 period. Underscoring the similarities of the two major multi-year developments of deep convection, spanning 1987–1994 and 2012–2018, and their successive convective relaxation phases, we note similar declines of the intermediate layer oxygen content in 1996 and 2023. This observation, along with the previously noted in the will allow to better understand the dynamics of dissolved gases in the ocean and test marine biochemistry models.

Discussion and conclusions

Probing the deep-sea environment with autonomous platforms, and implementing innovative approaches to thorough processing, analysis, and synthesis of their data, streaming in massive quantities, allows us to make our full-ocean-depth variability and process studies more potent, more cost-effective, greener and, last but not least, more outreaching

The ship-based oceanographic measurements collected by the Bedford Institute of Oceanography exclusively during the period of 1990–2019, initially as part of the World Ocean Circulation Experiment (WOCE) and recently in support of the Deep-Ocean Observation and Research Synthesis (DOORS), were of an exceptionally high quality that allowed us to track convective signals spreading from the Labrador Sea across the ocean^{10–12,14,15}. However, the advances made over the first decades of the twentieth century in how the ocean is sampled and analyzed, call for a revision of the relative roles of the ship-based observation in a wide range of water-column state assessments, and process (e.g., convection) studies. The ship surveys conducted once a year are not sufficient for evaluation of seasonal, interannual, and longer-term changes in the upper, 0–200 m, and, to some degree, deeper parts of the water column (Fig. 3). Furthermore, the cost and environmental impact of every trip to a remote location need to be weighed against all anticipated unique deliverables and research gains. The present study shows how to improve the quality, completeness, and informativeness of oceanographic results while reducing the cost and carbon footprint of the underlying data collection. All available spatially and temporally abundant year-round Argo and emerging Deep Argo float observations, enhanced by the ship-based

measurements, are tested, quality-controlled, edited, calibrated, integrated, and analyzed through iterative optimization. This method allowed me to reduce the dependence of the resulting real-time full-depth ocean state assessment on ship data quality and availability. In particular, the ship data absence in 2017 and 2021, and the drop in quality after 2019 did not affect our results for these years.

Intensifications (deepening) and relaxations (shoaling) of deep convection are collectively controlled by surface cooling, preconditioning and restratification

By analyzing the factors affecting the strength and depth of winter mixing, and mixed-layer properties, I show that both single mixing events and multiyear convective intensification–relaxation cycles are controlled by the joint action of three processes. Predominantly local winter surface cooling spins up a convective cycle. Local and possibly remote (e.g., though LSW recirculation) preconditioning or retention of reduced vertical stability imposed by the previous convections prolongs convective development. Advective-diffusive originating from multiple remote sources, post-convective seasonal-to-interannual restratification impedes, ultimately stopping, convection. These three factors take turns in determining the outcome of each convective event.

The deepening phase of the studied 2012–2023 convective cycle lasted 7 years—in four (2012–2015) it was led by cooling, and in the other 3 years (2016–2018) by preconditioning.

Next came the relaxation phase, which ended with two convective shutdowns (in 2021 and 2023) separated by a moderately deep convection (in 2022). The 2021 and 2023 shutdowns were imposed by a 2014–2023 WSHL low, and a massive freshening of the Labrador Sea, respectively.

Stratospheric and tropospheric circulation changes led to the shutdown of convection in 2021

In 2015 and 2022, the deepened, intensified, and spatially overlapped stratospheric, PV, and tropospheric, IL, circulation, and low-pressure systems made the westerlies stronger, WSHL higher, and Labrador Sea convection deeper. The collocation of these low-pressure systems leads to their mutual intensification and therefore can be used as a precursor of deep ocean convection.

In 2010 and 2021, by contrast, the disrupted, weakened, and spatially distanced PV and IL gave warm winter conditions with reduced surface cooling and convection depths (Figs. 5–7). When PV weakens, collapses, and shifts away from IL, the air mass over IL increases, weakening IL and, like in 2010 and 2021, shifting it southwest of its climatological position (Supplementary Note 7). In turn, the displaced IL weakens and even reverses the westerly winds consequently reducing WSHL over the Labrador Sea.

Similarly to the atmospheric situation that led to a shutdown of deep convection in 2010, PV disrupted and collapsed, and its weakened fragments (flattened depressions in the 50 mbar geopotential surface) relocated toward Siberia in January 2021. At the same time, the weakened Icelandic Low shifted southwest. The displacement of the two lows reversed the westerly winds, which in turn reduced WSHL.

Even though PV was also disrupted in the winter of 2023, this was not the main reason for an even stronger shoaling of convection and, consequently, the recently progressed convective shutdown.

The largest Labrador Sea freshening of the past five decades, caused by the extreme Arctic sea ice losses and Beaufort Gyre freshwater release, was the reason for the shutdown of convection in 2023

The 2021–2023 freshening (Figs. 2–4, 8–10) that is presently spread over the upper half of the intermediate layer was a direct response to the anomalously high Arctic sea ice losses registered in 2019 and 2020 (Figs. 8 and 9). Furthermore, the 2015–2022 mean summer ASIEVA was the lowest 8-year means on record, emphasizing the cumulative effect of the recent Arctic sea ice loss. Large-scale implications of this rapidly developing salinity anomaly are yet to be seen, but the fact that the Labrador Sea incurred its second

record shallow convection in 2023 is said to be the first observed impact of the recently accelerated Arctic ice retreat on the deep sea environment. Consequently, 2023 was the year, when the Labrador Sea first experienced a significant impact of Global Warming on its winter convection and associated environmental conditions.

The massive BGFW release, obvious from the BGFW content decline, ongoing since 2017 and enhanced by the accelerated ASIEVA reductions in 2019 and 2020, is likely to further expand the effect of the warming and deicing Arctic on the CLS freshwater content, convection, and ventilation.

Accelerated melting of Greenland ice could also contribute to the Labrador Sea freshening. However, this source may not be sufficient to cause a rapid voluminous sea-wide freshening^{43,44}. Furthermore, the recent low-salinity anomaly was spreading along the AR7W line from west to east (e.g. Fig. 2). This means that the present freshwater anomaly entry point might be located anywhere from the Labrador Shelf to Davis Strait, connected to either Arctic or Hudson Bay origin. Both Greenland and Hudson Bay sources are not ruled out as possible sources of the CLS freshening. However, given the magnitude and persistence of both recent seasonal ASIEVA changes and ongoing BGFW release (Figs. 8 and 9), jointly shaping the Arctic freshwater outflow, the latter is likely the reason for the massive Labrador Sea freshening and resulting 2023 convective shutdown.

Similarly to the last and most massive freshening on record, the Labrador Sea freshening events of 2008–2009 and 2013–2015 can be linked to the extreme Arctic sea ice losses in 2007 and 2012, respectively (Fig. 9). However, their impacts on winter convection were weaker than that observed in 2023.

Fully documented and analyzed, the 2012–2023 convective cycle sets a critically important benchmark for deep ocean variability, connectivity, climate, and ecosystem studies

2021 featured the shallowest convection in more than a decade, sharply ending the deepest multiyear convective cycle since the mid-1990s (Figs. 8 and 10). Being followed by a year (2022) with extreme winter cooling and twice deeper convection, 2021 inflicted spikes in all analyzed watermass characteristics (Fig. 4). Convection shoaled even more two years later, in 2023, reaffirming the previous end-cycle/shutdown point. Considering that the Labrador Sea is the source of LSW, serving as a vehicle for the subpolar climate signals spreading across the deep ocean, these spikes and associated trend reversals present reliable references or benchmarks for follow-up ocean variability, mixing, water-mass spreading¹⁵ and overturning circulation^{26,27,45} investigations. The LSW_{2012–2018}–NEADW salinity signal transfer, shown in Fig. 10 and explained in the “Results” section, sets a starting point in this direction. The freshening signal transferred from LSW_{2012–2018} to NEADW (possibly over or by the Mid-Atlantic Ridge) returned to the Labrador Sea at a greater depth 6–7 years later (Fig. 10). More than 30 years ago, LSW_{1987–1994} transferred its fresh pulse to NEADW, which NEADW delivered back to the Labrador Sea, showing it there at a comparable depth with a comparable delay (Fig. 10, also see¹⁹ for details).

The ocean and climate research community will benefit from the findings presented in this article in many ways, among which are the following. By aligning the documented Labrador Sea hydrographic changes with signals registered in other regions, the causes and implications of deep-water changes can be better diagnosed and understood. The revealed and analyzed intensifiers and inhibitors, drivers and stoppers, and outcomes of each Labrador Sea convective development advance our understanding of the climatological and environmental functions and significances, processes and trends, and last but not least, contribution to AMOC of the Labrador Sea.

Methods

Data sources

Our data sources include temperature and salinity observations from the profiling Argo floats for the period of 2002–2023¹⁶; recent and historical

observed-level temperature, salinity, and dissolved oxygen data from national and international ship-based surveys⁶⁷; a near-bottom temperature time series from a long-term mooring maintained by the Bedford Institute of Oceanography (BIO) on the upper Labrador Slope (Fig. 1b); the winter (January–March) NAO and AO indices; reanalysis-based turbulent and radiative heat flux components, air temperature, sea level pressure, and geopotential height from the U.S. National Centers for Environmental Prediction (NCEP); daily Arctic sea ice extent and volume values; and ship-based and McLane Moored Profiler measurements from the Beaufort Gyre Exploration Project⁴².

The Labrador Sea hydrographic observations became reasonably systematic in the late 1940s. For more than two and a half decades the International Ice Patrol, other U.S. Coast Guard surveys, and year-round Ocean Weather Ship Bravo patrols provided sufficient data to resolve decadal variability in the region (Supplementary Fig. 1). The field effort was enhanced by dedicated research missions usually conducted in winter, including the 1962 Erika Dan cruise, 1966 subpolar expedition led by John Lazier on CSS Hudson, and 1976 winter convection survey led by Allyn Clarke also on CSS Hudson. The major field programs and projects that contributed to the Labrador Sea research are well acknowledged in literature (e.g. refs. 1,6). Even though both seasonal and spatial data coverage changed considerably over time (Supplementary Fig. 1), the layer-average temperature and salinity maps shown in Fig. 1c–e and Supplementary Figs. 6–8 reveal high homogeneity of seawater properties across the central Labrador Sea that allowed me to accurately define the convection zone for the purposes of data selection and averaging (Fig. 1b).

Until the mid-1980s, the main source of reliable deep-sea pressure (depth), temperature, and salinity measurements remained unprotected and protected reversing thermometers, and water sample salinity determinations. A new era with respect to oceanography data quality started in 1990.

Ship-based observations during the World Ocean Circulation Experiment and beyond.

In July of 1990, the Bedford Institute of Oceanography (BIO) of Fisheries and Oceans Canada conducted the first occupation of the Atlantic Repeat Hydrography Line 7–West (AR7W) line as part of the World Ocean Circulation Experiment (WOCE) deployed in the same year^{4–6}. Spanning approximately 900 km, the AR7W line crosses the Labrador Sea from Misery Point on Labrador to Cape Desolation on Greenland (Supplementary Note 2, Supplementary Table and Fig. 1). In addition to the annual BIO surveys, the AR7W line was occasionally occupied by other organizations signifying the importance of the Labrador Sea for the understanding of the processes, dynamics and climate variability and change in the subpolar North Atlantic (e.g. ^{1,4–6,12,16,17,20,24,26,43,47,48}). The highest accuracy achievable in the modern measurements of temperature (<0.002 °C) and salinity (<0.002) was maintained and exceeded for the AR7W during the WOCE (1990–2002), and until 2019, as part and in support of the Deep-Ocean Observation and Research Synthesis (DOORS) that I initiated and continually expanded, bringing new data sets international partnerships and regional and multidisciplinary linkages, improved and enhanced as a follow-up to the WOCE (Supplementary Note 2). Unfortunately, the ship-based component of the Labrador Sea DOORS project was discontinued at BIO after 2019, affecting the quality of the subsequent ship-based measurements.

The consistently high data quality allowed us to track the propagation of important deep-water signals across the subpolar North Atlantic^{10–12,19} and toward the Equator^{14,15,49}.

The 2010–2023 temperature, salinity, and density sections constructed from the ship-based observations on the repeat hydrography line AR7W across the Labrador Sea are shown in Supplementary Figs. 2–4 and discussed in Supplementary Note 3.

For this study, the AR7W archive, with the last examples was enhanced with profiles from nearby locations shown as point clouds in Fig. 1.

Profiling Argo float data. The advancement of the international Argo program largely reduced our dependence on ship-based observations for mapping and studying processes and interannual variability in the Labrador and other deep basins (Supplementary Notes 4 and 5). The year-round 0–2000 m *Standard-Argo* and full-depth *Deep-Argo* float profiles improve the ongoing annual ocean state assessments both quantitatively and qualitatively and replace ship-based observations absent in some years (e.g., 2017 and 2021 in this work). Moreover, Argo makes it possible for us to solve the tasks unattainable with the ship-based data alone, including investigation of seasonal processes and variability, especially, during winter, when ship surveys are not normally present. The present study, as well as many other advancements recently made in the understanding of the physical processes and seasonal-to-decadal scale variability in the Labrador Sea would not happen without Argo (we deployed the first Argo float in the Labrador Sea in July of 2002).

Atmospheric data: the North Atlantic and Arctic Oscillation indices.

The North Atlantic Oscillation (NAO) is an important teleconnection pattern influencing atmospheric processes in the Labrador Sea^{50,51}. A positive NAO or, essentially, an increased sea level pressure (SLP) difference between the Icelandic low-pressure system, which typically expands toward the Arctic during this NAO phase, and the high-pressure system over the Azores and subtropical Atlantic, intensifies the westerlies bringing anomalously cold dry continental air to the northwestern North Atlantic, including the Labrador Sea. In turn, a negative NAO, associated with a decreased SLP difference between the two systems, weakens the westerlies bringing warmer-than-average conditions. The NAO phase changes control the large-scale transports of heat and moisture in the polar and subpolar regions. On the other hand, the NAO index changes are associated with changes in the intensity and location of the atmospheric jet stream and storm track, and, as shown here (Figs. 5–7), the intensity, size, and location of the polar vortex. The winter NAO index series shown in Figs. 4, 5, and 8 are produced by averaging the December-to-March principal component-based NAO index values obtained by applying the first empirical orthogonal function to the 700-mbar height anomaly fields for the Northern Hemisphere (<https://www.cpc.ncep.noaa.gov/products/precip/CWlink/pna/nao.shtml>).

The winter Arctic Oscillation or Northern Hemisphere annular mode index (https://www.cpc.ncep.noaa.gov/products/precip/CWlink/daily_ao_index/ao.shtml) is discussed in Supplementary Note 7 and *Atmospheric Factors*.

Atmospheric data: heat flux components, air temperature, sea level pressure, and geopotential heights. The spatiotemporal arrays of the atmospheric variables and derived winter forcing indices brought together in this study are based on the National Centers for Environmental Prediction (NCEP) and the National Center for Atmospheric Research (NCAR) Reanalysis dataset⁵², provided by the National Oceanic and Atmospheric Administration, Boulder, Colorado, USA. The two reanalysis products, R1 and R2, of the highest resolution available (e.g., 6 h) are being compared for achieving best performance, and jointly used to achieve the most extensive and detailed up-to-date atmospheric data coverage.

Arctic sea ice extent and volume. The daily Arctic sea ice extent and volume (ASIEV) values were obtained from the National Snow and Ice Data Center (<https://nsidc.org/home>) and Polar Science Center (<https://psc.apl.uw.edu/research/projects/arctic-sea-ice-volume-anomaly>), respectively. The ASIEV anomalies (ASIEVA) are obtained by interpolating the ASIEV series over small data gaps (10 days), computing the 1979–2022 daily means using only the years without omissions, and subtracting the 1979–2022 mean from respective daily values. Then, ASIEVA is averaged over February–March (late-winter) and August–October (late-summer) periods of the calendar years and their difference are computed.

Data processing

The historical shipboard oceanographic observations, including, water samples, reversing thermometer, and shipboard CTD data, have been quality controlled, edited, and processed following the steps of⁵³.

For the period of 1990–2019, the AR7W and other Labrador Sea ship-based pressure, temperature, conductivity, salinity, and dissolved oxygen observations have been quality controlled and calibrated to meet and mostly exceed the WOCE data quality standards (0.001 °C for temperature and 0.0015 for salinity achievable by DOORS). Each sea mission's dataset has been calibrated using the laboratory calibrations of pressure, temperature, and conductivity sensors, as well as excessively large quantities (on the order of a thousand per variable) of accurately determined water-sample salinity (Autosal) and dissolved oxygen (Winkler titration) concentration values, and <0.001 °C-accurate temperature readouts obtained at all water sampling depths with an SBE35 temperature recorder.

The data processing and analysis techniques that I developed and implemented through the studied period clearly demonstrate how the quality and accuracy of the Argo float observations can be further improved, expanding the range of uses and applications of the most comprehensive oceanographic data set of the 2002–2023 period. (These methods can be also adapted to any other massive autonomous-platform-based, e.g., sea glider, a data stream). On the other hand, the present paper, enhanced by Supplementary Notes 1–6, provides evidence of a substantial reduction of our dependence on the expensive, infrequent, seasonally biased, and leaving large carbon footprint, ship-based observations, which were earlier used for studying both processes and variability across the ocean. Particularly, two years, 2017 and 2021, set important precedents, in which, despite the complete lack of ship-based observations, the off-shelf region of the Labrador Sea was fully and continuously monitored and studied (in fact, 2021 was a critical year for the Labrador Sea processes and variability). Sufficient year-round coverage of Deep, Standard, and Biological Argo float profiles passed through thorough quality-control and time-drift correction, as outlined below and in Supplementary Notes 4 and 5, provided a reliable basis for mapping the seasonally-unbiased ocean states in these years.

Profiling Argo float data quality control, editing, and time drift and shift evaluation and correction system. One of the components of the Argo data processing system that I developed is the minimization of offsets and drifts in mixed Real-Time and Delayed Mode data collections. It was essential for achieving both completeness and the quality of results presented in this study and can be also adapted for other regions and even instrument types. Therefore, I split the description and illustration of the technique between the “Methods” section and Supplementary Notes 4 and 5.

Each update or addition of observations and data control and analysis procedures is followed by reprocessing of the entire set of year-round Argo temperature, salinity, and density (henceforth, *property*) measurements, including two-step quality control—*Data Editing and Cleaning* and *Property Drift Correction*. As the first step, I perform automated, semiautomated, and visual detection of faulty uncorrectable (beyond calibration) profiles, bad data segments, and isolated outliers and their subsequent elimination. For the second step, I implemented a novel approach to the detection and correction of instrumental drifts and shifts in consecutive series of vertical profiles and fixed-point measurements collected by Argo floats, ships, sea gliders, moorings, and other platforms. Preferred, but not required, for this method to have observations reaching deeper than 500 m.

The concept of drift detection, optimization, fitting, and correction is based on extensive inter-comparisons of sequential observations collected by each float with all other multiplatform observations. Processing, one by one, all floats found in the extended study domain (Supplementary Figs. 5–8), my specially-designed computer algorithm (which is ready to be adapted to other regions) performs cross-comparisons of individual profiles with all other profiles (either including or excluding those from the same float) meeting certain regional, bathymetric and temporal criteria. The analysis is performed for three or more independent vertical layers, with all steps of the process repeated iteratively

for the whole profile collection until the outcome, containing recommended correction, is stable and robust.

In a computationally faster version of the drift detection and correction method, instead of comparing each float's profiles with all other floats' profiles selected by certain criteria, the profiles are projected on and compared against specially designed multidimensional *reference fields* (Supplementary Figs. 9, 10). The property reference fields are recurrently generated from scratch for each *vertical layer* and each of, presently, seven overlapping *geographic regions* (Supplementary Figs. 5–8) by averaging the multiplatform observations in regional-bathymetric-vertical-time bins at each iteration. *Geographic region*, *vertical layer boundaries*, *water depth*, and *decimal year* are used here as independent variables when building the reference fields from the respectively bin-averaged layer-averaged values, and when cross-matching and comparing with the individual-profile layer-averaged values. Importantly, the bin-averaging is performed on the incrementally corrected observations, with all new additions, modifications, and deletions of corrections instantly applied.

The reference regions are characterized by spatial uniformity of properties within their individual bathymetric ranges (Supplementary Figs. 5–8). The reference layers are defined by minimizing the vertical and horizontal uniformities and gradients for each property throughout each region. The present choice of three layers, among other advantages allows testing the accuracy of pressure corrections applied to temperature and salinity measurements.

As the next step, layer-by-layer, each profile's layer-average property is subtracted from all reference values matched in the *vertical layer*, *region*, *water-depth* and *decimal-year* coordinates. Since the regions overlap, a single profile can be pinned to more than one regional reference field. Each reference field that includes the profile location is presented as a function of *water-depth* and *decimal-year*, and is interpolated to the *water-depth* and *decimal-year* of the analyzed profile using either bilinear, closest-neighbor, or weighted-averaging method. The deviations from all matched regional references are then averaged to produce a deviation of the tested layer-average property from the collective reference.

For each float, property, and vertical layer, a time series of deviation from the collective reference field is constructed (e.g., Supplementary Figs. 11–13). An assessment or, if after the first iteration, reassessment of data quality is performed, and all instructions required for subsequent data elimination, and shift or drift correction are added to the list of Argo data processing instructions. Each such instruction includes property name, correction or elimination action requested, start date, end date, depth range, property range, value of correction, rate of correction, and comment (details in Supplementary Note 4).

The other action request that can be listed in the processing instructions is bad data exclusion requests also by float, property, decimal year range, depth range, and property range. Obviously, this formulation allows the exclusion of a single-point outlier, a data segment, or an entire profile, again cumulatively.

After applying all requested corrections to the entire data set, the region- and layer-specific water-depth and decimal-year dependent reference fields are regenerated from scratch, and a new iteration of data quality testing and improvement is performed, including updating the processing instructions. The iteration continues until there is no new instruction added to the list, and no data modified or added.

Depending on the data source and quality level, each profile is given a weight used in bin-averaging. Properly calibrated ship-based observations (e.g., the 1990–2019 WOCE and DOORS surveys) are given the highest weights, while float data with high noise levels and strong uncorrected sensor drifts receive considerably lower weights. Regarding the Argo data, Delayed Mode profiles are chosen if available, otherwise Real-Time profiles are used. However, the quality flags provided by the national data centers and distributed with the data are ignored as all profiles are being recurrently and thoroughly examined, edited, and corrected by the present system conducting numerous tests carefully tuned and customized for the studied region.

The application of the outlined approach to data cleaning and sensor drift correction substantially improved the temporal and spatial consistency of the observations from different floats and ship surveys, as reflected in the quality of the data products and results presented in this article.

Spatiotemporal synthesis of profiling float and ship survey data. A new method was developed to construct vertical section plots along any arbitrary-chosen line (defined by two points) or polyline (defined by three or more points) crossing a prominent important topographic feature, a bathymetrically challenging region, or an entire ocean basin. This method uses a *hybrid-coordinate* system for spatial data projection. It blends all accessible multiplatform profiles that meet any interactively-set decimal-year, seasonal, water-depth, and profile-depth range criteria, and is located either within a certain distance range of the line or within/outside predefined inclusive/exclusive polygons. The spatial criteria are combined using the union and intersection rules. The distance range criteria can be based, for example, on the extent of the convection zone measured across the line (200 km based on Fig. 1c–e and Supplementary Figs. 6–8). Inclusive polygons may outline shapes of studied objects, e.g., the convection zone, while exclusive polygons avoid topographic obstacles near the section line, e.g., Eirik Ridge. Both distance range and inclusive/exclusive polygon-based spatial criteria were jointly used to construct the composite sections presented in Fig. 2.

All profiles matching the specified criteria are selected and projected on the chosen line or polyline. Each vertical profile is assigned a pair of horizontal coordinates comprising the distances along and from the section line (in the case of polylines the shortest projection is chosen). The first coordinate refers to the position of the profile on the section measured from one of its ends. The second coordinate (the shortest profile-to-line distance), reflecting the spread of profiles away from the line, enters the mentioned distance range selection criteria chosen in combination with the polygon criteria.

The key new feature of the *hybrid-coordinate* vertical section construction technique is its ability to switch between three or more different distance computation schemes. The choice of scheme is dictated by water depth, region, and location. Figure 1a depicts this approach for the AR7W line chosen as the reference for the present multiplatform data synthesis. The locations of the selected profile are color-coded by the along-section distance, obtained as follows:

- All profiles from within the bathymetric range of the *continental slope* (here, 600–2800 m) are projected onto the AR7W line by following their respective bathymetric contours until crossing the reference line (AR7W) at bathymetrically-defined along-section distances.
- All profiles from within the *central* region (>3300 m) are projected onto the line following the shortest-distance or normal projection rule, giving direct or shortest distances.
- All *transitional* profiles (2800–3300 m) have their along-line distances computed as weighted means of their respective “bathymetric” and “shortest distance” distances, linearly blending the two projections with the weights respectively declining/increasing from 1/0 to 0/1 throughout the transition.

For depths shallower than 600 m, the normal shortest-distance projection scheme is chosen for the shelf (<300 m), and the transitional or blended deeper (300–600 m).

The resulting along-line (i.e., monotonically increasing along-the-line) distances combined with the depths of vertically interpolated profile values are used to construct presentable section plots from randomly scattered data over the boundary.

Overall, my new approach to vertical section plotting is rationalized by two principles: (1) the bathymetry-following distances account for strong topographic control of the boundary currents thus improving representation of oceanography over the continental slope and rise in the resulting section plots in comparison with the normal (shortest-distance) projection

based distances; (2) uniformity of seawater properties and weak horizontal gradients across the central part of the section line (where the normal projection is used), and along the continental slope (where the bathymetry-following and blended projections are used), allow to consolidate more data from a reasonably wide range of distances from or to the line without distorting the resulting section plots, while increasing the statistical significance of the resulting section point values.

Exploring deep ocean features and variability—from ship surveys to Deep Argo. Deep Argo has been massively providing full-depth Labrador Sea property profiles since 2020. With the aforementioned quality control, time drift correction, and quality validation procedures applied, these profiles become a workable alternative to the expensive, seasonally biased expensive, massive their carbon footprint, ship survey observations (Supplementary Figs. 14–16). For the purposes of this study, the ship-based observations have been fully replaced with Argo and Deep Argo profiles in 2017, 2021, and 2021, respectively. The Deep Argo covers the Labrador Sea for the entire water depth, including its deepest locations (>4000 m).

A total of 15 Deep Argo floats surveyed the Labrador Sea, at least episodically, over the period of 2020–2023. The Deep Argo array is expected to grow providing sufficient data coverage for continuous accurate mapping of the critical seawater properties below 2000 m, reducing our dependence on the ship-based observations for this part of the water column as well.

Data selection and time-bin averaging in the central Labrador Sea. Defining the central Labrador Sea (CLS) as the region where above-average winter surface heat losses (WSHL) are likely to result in deep convection, its boundaries are adapted from refs. 7,8. The CLS quality-controlled ship-based and Argo float profiles are indicated in Fig. 1b, with dark-red dots. The respective individual CLS profile values from 1000 and 1500 m are shown in Fig. 4. Overall, any fixed-depth CLS oceanographic property sampled near-instantaneously below 500 m shows very little scatter, affirming the representation of the LSW source region with the presently chosen CLS. Furthermore, the robustness of the point-cloud signals makes the corresponding time-bin-averaged values and profiles an accurate representation of the weekly-to-annual CLS conditions. This approach provides a basis for close and detailed tracking of the recurring seasonal development (Fig. 3) and depicting long-term cycles and trends in convective developments (Figs. 4, 8–10).

Time-depth series of spatially averaged Argo float and ship-based properties with a vertical resolution of 5 m, a temporal resolution of 2.5 days, and a temporal search range varying from 6 to 11 days, dependent on data availability and density, have been computed for the CLS region, with the area of about 60,000 km² (Fig. 1, right), for the period of 2002–2023 (Fig. 3). The annually-averaged full-ocean-depth CLS temperature, salinity, density, and dissolved oxygen profiles, presented in the time-depth and temperature-salinity coordinate systems (Fig. 10), allow to rank all major multiyear convective developments in the Labrador Sea by their duration, strength, and depth over 76 years, 1948–2023.

Construction of annual vertical profiles. The 2017 and 2021 annually averaged CLS profiles are exclusively based on the Argo data, due to the absence of ship surveys in these years. Otherwise, the annual vertical profiles are compiled from the ship observations.

The quality controlled and calibrated to high accuracy ship-based observations are averaged on constant density (isopycnal) surfaces annually from 1987 to 2023, except for 2017 and 2021. In turn, the 2017 and 2021 April-to-August Argo observations are averaged on constant pressure (isobaric) or depth surfaces annually and merged with the rest of the annual profiles. The reason for not using isopycnal averaging for the corrected Argo data is that any small residual errors may affect density. Alternatively, the Argo profiles can also be averaged using the next, hybrid, method. The pre-1987 ship-based CLS temperature and salinity observations are processed by

applying a hybrid two-step averaging method to each annual data set—first, isobaric averaging is performed in overlapping spatiotemporal bins; then, isopycnal averaging is applied to the pre-averaged profiles from within CLS or any other region of choice.

Winter surface heat losses and ocean heat content changes. The net surface heat flux (NSHF) values are computed by adding up the incoming and outgoing shortwave and longwave radiative fluxes, and the turbulent latent and sensible heat fluxes (total of six sea-surface heat flux terms), extracted from the 6-hourly NCEP/NCAR Reanalysis fields, and then averaging over the central Labrador Sea (Fig. 1, right, scattered dark-red dots).

Each cooling or winter season is identified individually in a NSHF series following the approach introduced in our earlier publications^{7,8,35}. Its start and end points are associated with the fall and spring NSHF sign reversals (changeovers), i.e., the moments when the sea-to-air NSHF switches to persistently positive in late fall and persistently negative in early spring, respectively. The total or cumulative surface heat loss (WSHL) incurred by the CLS in the identified cooling period is computed by integrating the CLS NSHF from its start to end. Short-term NSHF reversals having no impact on the total heat loss are ignored.

The total heat content losses incurred by the 15–2000 m layer of the CLS in all 2002–2023 cooling seasons are estimated in three steps: (1) a heat content time series is computed for the layer using the 2.5-day average temperature profiles (Fig. 3); (2) the start and end points of the layer cooling seasons are detected from respective tendency changeovers; (3) the heat content changes are integrated over the identified cooling seasons.

The CLS WSHL and 15–2000 m layer heat loss series are shown in Figs. 4 and 5.

Computation of convection depth. The depth of winter convection (included in Figs. 3–5, 8–10) is represented by the 75th percentile⁷ of the mixed layer depths achieved at the end of a chosen convective development or, if winter data are not present, after. Individual profiles with a definable fully-developed winter mixed layer are used in the evaluation of the metrics of each winter convection.

Data availability

Continuously updated, enhanced and improved data, and related instructions are available from the author (Igor Yashayaev, emails: Labrador.Sea@gmail.com; Igor.Yashayaev@dfo-mpo.gc.ca) upon reasonable request. The recent versions of the data files are available through Figshare: https://figshare.com/articles/dataset/Labrador_Sea_gridded_fields_and_time_series/25093262.

Code availability

Continuously updated, enhanced and improved codes and related instructions are available from the author.

Received: 25 May 2023; Accepted: 29 February 2024;

Published online: 27 March 2024

References

1. Yashayaev, I., Seidov, D. & Demirov, E. A new collective view of oceanography of the Arctic and North Atlantic basins. *Prog. Oceanogr.* **132**, 1–21 (2015).
2. Clarke, R. A. & Gascard, J.-C. The formation of Labrador Sea Water. Part I: large-scale processes. *J. Phys. Oceanogr.* **13**, 1764–1778 (1983).
3. Gascard, J.-C. & Clarke, R. A. The formation of Labrador Sea Water. Part II. Mesoscale and smaller-scale processes. *J. Phys. Oceanogr.* **13**, 1779–1797 (1983).
4. Lazier, J., Hendry, R., Clarke, A., Yashayaev, I. & Rhines, P. Convection and restratification in the Labrador Sea, 1990–2000. *Deep-Sea Res. I* **49**, 1819–1835 (2002).

5. Yashayaev, I. Hydrographic changes in the Labrador Sea, 1960–2005. *Prog. Oceanogr.* **73**, 242–276 (2007).
6. Kieke, D. & Yashayaev, I. Studies of Labrador Sea Water formation and variability in the subpolar North Atlantic in the light of international partnership and collaboration. *Prog. Oceanogr.* **132**, 220–232 (2015).
7. Yashayaev, I. & Loder, J. W. Recurrent replenishment of Labrador Sea Water and associated decadal-scale variability. *J. Geophys. Res.: Oceans* **121**, 8095–8114 (2016).
8. Yashayaev, I. & Loder, J. W. Further intensification of deep convection in the Labrador Sea in 2016. *Geophys. Res. Lett.* **44**, 1429–1438 (2017).
9. Talley, L. D. & McCartney, M. S. Distribution and circulation of Labrador Sea Water. *J. Phys. Oceanogr.* **12**, 1189–1205 (1982).
10. Yashayaev, I., Bersch, M. & van Aken, H. M. Spreading of the Labrador Sea Water to the Irminger and Iceland basins. *Geophys. Res. Lett.* **34**, 1–8 (2007).
11. Yashayaev, I., van Aken, H. M., Holliday, N. P. & Bersch, M. Transformation of the Labrador Sea water in the subpolar North Atlantic. *Geophys. Res. Lett.* **34**, 1–8 (2007).
12. Yashayaev, I., Holliday, N. P., Bersch, M. & van Aken, H. M. The history of the Labrador Sea water: production, spreading, transformation and loss. In *Arctic–Subarctic Ocean Fluxes: Defining the Role of the Northern Seas in Climate* (eds Dickson, R., Meincke, J. & Rhines, P.) 569–612 (Springer, Dordrecht, 2008).
13. Kieke, D., Klein, B., Stramma, L., Rhein, M. & Koltermann, K. P. Variability and propagation of Labrador Sea Water in the southern subpolar North Atlantic. *Deep Sea Res. Part I* **56**, 1656–1674 (2009).
14. Le Bras, I. A., Yashayaev, I. & Toole, J. M. Tracking Labrador Sea Water property signals along the Deep Western Boundary Current. *J. Geophys. Res.: Oceans* **122**, 5348–5366 (2017).
15. Chomiak, L. N., Yashayaev, I., Volkov, D. L., Schmid, C. & Hooper, J. A. Inferring advective timescales and overturning pathways of the Deep Western Boundary Current in the North Atlantic through Labrador Sea Water advection. *J. Geophys. Res.: Oceans* **127**, 1–23 (2022).
16. Dickson, R. R. et al. Rapid freshening of the Deep North Atlantic over the past four decades. *Nature* **416**, 832–837 (2002).
17. Curry, R., Dickson, R. R. & Yashayaev, I. A change in the freshwater balance of the Atlantic Ocean over the past four decades. *Nature* **426**, 826–829 (2003).
18. Dickson, R., Curry, R. & Yashayaev, I. Recent changes in the North Atlantic. *Philos. Trans. R. Soc. Lond. Ser. A* **361**, 1917–1934 (2003).
19. Yashayaev, I. & Dickson, R. R. Transformation and fate of overflows in the northern North Atlantic, In *Arctic–Subarctic Ocean Fluxes: Defining the Role of the Northern Seas in Climate* (eds Dickson, R., Meincke, J. & Rhines, P.) 505–526 (Springer, Dordrecht, 2008).
20. van Aken, H. M., de Jong, F. & Yashayaev, I. Decadal and multi-decadal variability of Labrador Sea Water in the north-western North Atlantic Ocean derived from tracer distributions: heat budget, ventilation, and advection. *Deep-Sea Res. I* **58**, 505–523 (2011).
21. Tesdal, J.-E., Ducklow, H. W., Goes, J. I. & Yashayaev, I. Recent nutrient enrichment and high biological productivity in the Labrador Sea is tied to enhanced winter convection. *Prog. Oceanogr.* **206**, 1–22 (2022).
22. Curry, R. G. & McCartney, M. S. Ocean gyre circulation changes associated with the North Atlantic Oscillation. *J. Phys. Oceanogr.* **31**, 3374–3400 (2001).
23. Kostov, Y., Messias, M. J., Mercier, H., Johnson, H. L. & Marshall, D. P. Fast mechanisms linking the Labrador Sea with subtropical Atlantic overturning. *Clim. Dyn.* **60**, 2687–2712 (2023).
24. Rhein, M. et al. Deep-water formation, the subpolar gyre, and the meridional overturning circulation in the subpolar North Atlantic. *Deep-Sea Res. II* **58**, 1819–1832 (2011).
25. Boessenkool, K. P., Hall, I. R., Elderfield, H. & Yashayaev, I. North Atlantic climate and deep-ocean flow speed changes during the last 230 years. *Geophys. Res. Lett.* **34**, 1–6 (2007).
26. Thornalley, D. J. R. et al. Anomalously weak Labrador Sea convection and Atlantic overturning during the past 150 years. *Nature* **556**, 227–230 (2018).
27. Lozier, M. et al. A sea change in our view of overturning in the subpolar North Atlantic. *Science* **363**, 516–521 (2019).
28. Rhein, M., Steinfeldt, R., Kieke, D., Stendardo, I. & Yashayaev, I. Ventilation variability of Labrador Sea Water and its impact on oxygen and anthropogenic carbon: a review. *Philos. Trans. R. Soc. A* **375**, 1–17 (2017).
29. Raimondi, L., Tanhua, T., Azetsu-Scott, K., Yashayaev, I. & Wallace, D. W. R. A 30-year time series of transient tracer-based estimates of anthropogenic carbon in the Central Labrador Sea. *J. Geophys. Res.: Oceans* **126**, 1–19 (2021).
30. LaBrie, R. et al. Deep ocean microbial communities produce more stable dissolved organic matter through the succession of rare prokaryotes. *Sci. Adv.* **8**, 1–12 (2022).
31. Hátún, H. et al. An inflated subpolar gyre blows life toward the northeastern Atlantic. *Prog. Oceanogr.* **147**, 49–66 (2016).
32. Hurrell, J. W. Decadal trends in the North Atlantic Oscillation: regional temperatures and precipitation. *Science* **269**, 676–679 (1995).
33. Zhou, S., Miller, A. J., Wang, J. & Angell, J. K. Trends of NAO and AO and their associations with stratospheric processes. *Geophys. Res. Lett.* **28**, 4107–4110 (2001).
34. Waugh, D. W., Sobel, A. H. & Polvani, L. M. What is the polar vortex and how does it influence weather? *Bull. Am. Meteorol. Soc.* **98**, 37–44 (2017).
35. Yashayaev, I. & Loder, J. W. Enhanced production of Labrador Sea Water in 2008. *Geophys. Res. Lett.* **36**, L01606 (2009).
36. E. Kenchington, I. Yashayaev, O. S. Tendal and H. Jørgensbye, Water mass characteristics and associated fauna of a newly discovered *Lophelia pertusa* (Scleractinia: Anthozoa) reef in Greenland waters. *Polar Biol.* **40**, 321–337 (2017).
37. Davis, P. E. D., Lique, C. & Johnson, H. L. On the link between Arctic Sea ice decline and the freshwater content of the Beaufort Gyre: insights from a simple process model. *J. Clim.* **27**, 8170–8184 (2014).
38. Li, H. & Fedorov, A. V. Persistent freshening of the Arctic Ocean and changes in the North Atlantic salinity caused by Arctic sea ice decline. *Clim. Dyn.* **57**, 2995–3013 (2021).
39. Timmermans, M.-L. & Toole, J. M. The Arctic Ocean’s Beaufort Gyre. *Annu. Rev. Mar. Sci.* **15**, 223–248 (2023).
40. Lin, P. et al. Recent state transition of the Arctic Ocean’s Beaufort Gyre. *Nat. Geosci.* **16**, 485–491 (2023).
41. Zhang, J. et al. Labrador Sea freshening linked to Beaufort Gyre freshwater release. *Nat. Commun.* **12**, 1 (2021).
42. Proshutinsky, A. et al. Analysis of the Beaufort Gyre freshwater content in 2003–2018. *J. Geophys. Res.: Oceans* **124**, 9658–9689 (2019).
43. Dukhovskoy, D. S. et al. Role of greenland freshwater anomaly in the recent freshening of the Subpolar North Atlantic. *J. Geophys. Res.: Oceans* **124**, 3333–3360 (2019).
44. Dukhovskoy, D. S. et al. Time scales of the Greenland Freshwater anomaly in the subpolar North Atlantic. *J. Clim.* **34**, 8971–8987 (2021).
45. Li, F. et al. Subpolar North Atlantic western boundary density anomalies and the Meridional Overturning Circulation. *Nat. Commun.* **12**, 3002 (2021).
46. Wong, A. P. S. et al. Argo Data 1999–2019: two million temperature-salinity profiles and subsurface velocity observations from a global array of profiling floats. *Front. Mar. Sci.* **7**, 1–23 (2020).
47. Fröb, F. et al. Irminger Sea deep convection injects oxygen and anthropogenic carbon to the ocean interior. *Nat. Commun.* **13244**, 1–8 (2016).

48. Holliday, N. P. et al. Ocean circulation causes the largest freshening event for 120 years in eastern subpolar North Atlantic. *Nat. Commun.* **11**, 1–15 (2020).
49. Smith, J. N., Smethie, W. M. Jr, Yashayev, I., Curry, R. & Azetsu-Scott, K. Time series measurements of transient tracers and tracer derived transport in the deep western boundary current between the Labrador Sea and the subtropical Atlantic Ocean at Line W. *J. Geophys. Res.: Oceans* **121**, 8115–8138 (2016).
50. Barnston, A. G. & Livezey, R. E. Classification, seasonality and persistence of low-frequency atmospheric circulation patterns. *Mon. Weather Rev.* **115**, 1083–1126 (1987).
51. Hauser, T., Demirov, E., Zhu, J. & Yashayev, I. North Atlantic atmospheric and ocean inter-annual variability over the past fifty years – dominant patterns and decadal shifts. *Prog. Oceanogr.* **132**, 197–219 (2015).
52. Kalnay, E. et al. The NCEP/NCAR 40-year reanalysis project. *Bull. Am. Meteor. Soc.* **77**, 437–470 (1996).
53. Yashayev, I. & Seidov, D. The role of the Atlantic Water in multidecadal ocean variability in the Nordic and Barents Seas. *Prog. Oceanogr.* **132**, 68–127 (2015).

Acknowledgements

The author is grateful to Bruce Carson and Richard Boyce, who during the WOCE field program were responsible for servicing our dedicated seawater property sensors and maintaining high-accuracy salinity measurements critically important for deep-sea observations. The officers and crews of the Canadian Scientific Ship and, recently, Canadian Coast Guard Ship Hudson, and, particularly, the commanding officers, James Strickland, William Naugle, Fergus Francey, and David Martin are commended for their contribution to the world-class Labrador Sea research. The present state-of-art synthesis of the seasonal-to-interdecadal variability in the key ocean region is dedicated to Bob Dickson (1941–2019), John Lazier (1936–2021), and Allyn Clarke (1943–2023). These great North Atlantic observational oceanographers laid the critical cornerstones of the present subpolar sea research, and through the last six decades inspired and influenced generations of researchers, including the author. The author thanks the anonymous reviewers for taking the time and effort necessary to review this paper. All corrections, comments, and suggestions provided by the reviewers were insightful, constructive, and fully and most gratefully used by the author to strengthen and enhance the study.

Author contributions

Igor Yashayev performed all steps of comprehensive *quality analysis, control* and iterative *reevaluation* (QACR) of all Argo float, mooring and ship-based temperature, salinity, and oxygen (TSO) measurements used in this study. QACR included point-to-point profile-to-profile series-to-series data

editing and cleaning, e.g., detection and removal of outlier and faulty segments; multifactor sensor calibrations, e.g., all deep-sea TSO observations collected by BIO since 1990, and instrumental bias and time-drift corrections, e.g., Argo TSO offsets and drifts; and reevaluation and validation of the data exclusions, calibrations and corrections. The author developed and implemented new methods for QACR and hydrographic variability and process studies; processed and analyzed the observations; visualized and interpreted the results; and prepared and revised the manuscript.

Competing interests

The author declares no competing interests.

Additional information

Supplementary information The online version contains supplementary material available at <https://doi.org/10.1038/s43247-024-01296-9>.

Correspondence and requests for materials should be addressed to Igor Yashayev.

Peer review information *Communications Earth & Environment* thanks the anonymous reviewers for their contribution to the peer review of this work. Primary Handling Editors: Viviane Menezes, Heike Langenberg. A peer review file is available.

Reprints and permissions information is available at <http://www.nature.com/reprints>

Publisher's note Springer Nature remains neutral with regard to jurisdictional claims in published maps and institutional affiliations.

Open Access This article is licensed under a Creative Commons Attribution 4.0 International License, which permits use, sharing, adaptation, distribution and reproduction in any medium or format, as long as you give appropriate credit to the original author(s) and the source, provide a link to the Creative Commons licence, and indicate if changes were made. The images or other third party material in this article are included in the article's Creative Commons licence, unless indicated otherwise in a credit line to the material. If material is not included in the article's Creative Commons licence and your intended use is not permitted by statutory regulation or exceeds the permitted use, you will need to obtain permission directly from the copyright holder. To view a copy of this licence, visit <http://creativecommons.org/licenses/by/4.0/>.

© Crown 2024